ELSEVIER

Contents lists available at ScienceDirect

Journal of Colloid And Interface Science

journal homepage: www.elsevier.com/locate/jcis



Regular Article



Time-resolved 2D and 3D imaging of hydrogen and brine displacement processes in porous Clashach sandstone

Eike M. Thaysen a,b,*, Ian B. Butler b, Aliakbar Hassanpouryouzband b, Catherine Spurin c, Damien Freitas b,d o, Roberto Rizzo b,e o, Fernando Alvarez-Borges f, Robert Atwood s, Katriona Edlmann b o

- ^a Department of Geosciences, Institute of Environmental Assessment and Water Research (IDAEA), Spanish Council for Scientific Research (CSIC), Jordi Girona 18–26, 08034 Barcelona, Spain
- b School of Geoscience, Grant Institute, The King's Buildings, The University of Edinburgh, James Hutton Road, Edinburgh EH9 3FE, United Kingdom
- ^c Department of Energy Science & Engineering, Stanford University, Palo Alto, CA, USA
- ^d University of Manchester, Diamond Light Source, Harwell Campus, Didcot OX11 0DE, United Kingdom
- e Department of Earth Sciences, Utrecht University, Princetonlaan 4, 3584 CB Utrecht, the Netherlands
- ^f µ-VIS X-ray Imaging Centre, Faculty of Engineering and Physical Sciences, University of Southampton, University Road, Southampton SO17 1BJ, United Kingdom
- ^g Diamond Light Source Ltd, Harwell Campus, Didcot OX11 0DE, United Kingdom

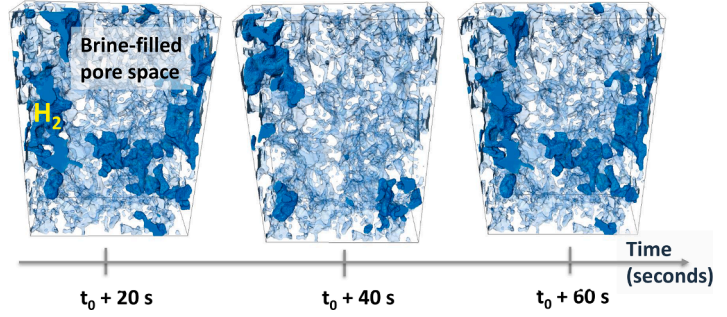
HIGHLIGHTS

H₂ displacement of brine includes sudden pore-filling events known as Haines jumps.

- \bullet Intermittent H_2 flow occurs in specific regions of the rock.
- A higher H₂ fractional flow increased the H₂ saturation from 20–22% to 28%.
- Phase connectivity appeared to have little control on H₂ saturation.

GRAPHICAL ABSTRACT





ARTICLE INFO

Keywords: Hydrogen Underground storage μCT Core flood experiments Haines jumps

ABSTRACT

Hydrogen (H_2) storage in porous geological formations offers a promising means to balance supply and demand in the renewable energy sector, supporting the energy transition. Important unknowns to this technology include the H_2 fluid flow dynamics through the porous medium which affect H_2 injectivity and recovery. We used time-resolved X-ray computed microtomography to image real-time unsteady and steady state injections of H_2 and brine (2 M KI) into a Clashach sandstone core at 5 MPa and ambient temperature. In steady state injections, H_2

Abbreviations: f, fractional flow; H_2 , hydrogen; IFT, interfacial tension; Kr, absolute permeability; kr, relative permeability; L, E and T, fitting parameters for the LET model; M, viscosity ratio; N_c , capillary number; S_w , water saturation; S_{nwi} , initial saturation; S_{nwr} , residual saturation; S_{wi} irreducible water saturation; χ , Euler characteristic; $\mu\chi$, mean Euler characteristic.

E-mail address: eike.thaysen@idaea.csic.es (E.M. Thaysen).

https://doi.org/10.1016/j.jcis.2025.137704

Received 27 November 2024; Received in revised form 11 April 2025; Accepted 24 April 2025 Available online 26 April 2025

^{*} Corresponding author at: Department of Geosciences, Institute of Environmental Assessment and Water Research (IDAEA), Spanish Council for Scientific Research (CSIC), Jordi Girona 18–26, 08034 Barcelona, Spain.

Intermittent flow Euler characteristic Relative permeability entered the brine-saturated rock within seconds, dispersing over several discrete pores. Over time, some H_2 ganglia connected, disconnected and then reconnected from each other (intermittent flow), indicating that the current presumption of a constant connected flow pathway during multiphase fluid flow is an oversimplification. Pressure oscillations at the sample outlet were characterized as red noise, supporting observations of intermittent pore-filling. At higher H_2 fractional flow the H_2 saturation in the pore space increased from 20-22~% to 28~%. Average Euler characteristics were generally positive over time at all H_2 flow fractions, indicating poorly connected H_2 clusters and little control of connectivity on the H_2 saturation. In unsteady state injections, H_2 displaced brine in sudden pore-filling events termed Haines jumps, which are key to understanding fluid dynamics in porous media. Our results suggest a lower H_2 storage capacity in sandstone aquifers with higher injection-induced hydrodynamic flow and suggest a low H_2 recovery. For more accurate predictions of H_2 storage potential and recovery, geological models should incorporate energy-dissipating processes such as Haines jumps.

1. Introduction

To reduce climate change we must implement passive and active carbon dioxide (CO₂) sequestration technologies (e.g. [1–3]), transition away from carbon (C)-based fuels, and make increased use of renewable

(zero C) energy [4]. Green hydrogen (H₂), produced by electrolysis of water using renewable energy, is proposed as key contributor to a zero or low C emission future due to its role as a promising energy carrier that could balance seasonal fluctuations in renewable electricity supply and demand [5,6]. Above ground storage of the large volumes of H₂ which

Table 1 μ CT-studies visualizing the H_2 distribution in sandstone. $\phi=$ porosity. Temp. = temperature.

S_{nwi} (%)	S_{nwr} (%)	Sandstone	Pressure (MPa)	Temp. (°C)	Sample preparation	Capillary number	φ (%)	Ref.
65	41	Gosford	0.1	20	NA	2.49×10^{-10} (drainage) 3.68×10^{-8}	18	[23]
53	44	Gosford	0.1	20	NA	(imbibition) 2.49×10^{-10} (drainage)	16	[24]
50-53	10-21*	Clashach	2-7	Ambient	Untreated	3.68×10^{-8} (imbibition) $1.7-6.8 \times 10^{-8}$ (drainage)	13- 14	[13]
17-53*	7-26*	Clashach, heterogeneous	10	50	Methanol-cleaned	$2.4-9.5 \times 10^{-6}$ (imbibition) 4.2×10^{-9} (drainage)	19- 28	[25]
30-44	10-11	Bentheimer	1	25	Untreated	2.3×10^{-6} (imbibition) 2.55×10^{-9} (drainage)	NA	[26]
30.	10	Bentheimer	1	Ambient	Untreated	2.62×10^{-7} (imbibition) 1.93×10^{-7} (drainage)	23	[27]
24-48 ^x	10-35 ^x	Bentheimer, slightly heterogeneous	10	50	Methanol-cleaned	5.79×10^{-9} (imbibition) 4.2×10^{-9} (drainage) 2.3×10^{-6}	23	[16]
76	40	Bentheimer	2.1	25	Cleaned with 50 % toluene/ 50 % methanol	(imbibition) 2.9×10^{-7} (drainage)	23	[28]
82	40-16*	Bentheimer	8	Ambient	Untreated	2.9 × 10 ⁻⁵ (imbibition) Drainage: capillary pressure controlled	20	[29]
-2-60	-0-45	Berea, heterogeneous	10	Ambient	Untreated	1.1×10^{-7} (imbibition) 9.1×10^{-9} (drainage)	20	[30]
41	36	Berea	3	30	NA	$1.1 imes 10^{-6}$ (imbibition) -10^{-8} (drainage)	18	[31]
44	32	Berea	5	25	Untreated	-10^{-6} (imbibition) 1.3×10^{-8} (drainage) 1.4×10^{-6}	18	[32]

[‡] Depending on pressure.

^{*} Depending on layer and/or injection/imbibition cycle.

^X Depending on layer and/or whether H₂-equlibrated brine or non-H₂ equilibrated brine was used.

are required to overcome renewable energy imbalances is impeded by the low volumetric energy density of H_2 [7]. Depleted gas fields and saline aquifers are considered among the most cost-effective options for large-scale H_2 storage [8], and recent findings suggest no major barriers to implementation [9–20].

Despite this, many of the different complexities of porous media H₂ storage have been insufficiently investigated [8]. Key challenges include understanding H₂ flow dynamics in porous media which, along with the behaviour of injected cushion gas, directly affects gas injectivity and recovery [8,19], and thus the economic viability of the storage operation. When H_2 is injected into a saline aquifer or a depleted gas field twophase flow of H₂ and brine can be expected [19], whereas injection into a depleted oil reservoir would further increase the complexity to threephase fluid flow. Visualization of the H₂ fluid flow at the pore scale provides crucial information about the fluid distribution and displacement mechanisms, which can be incorporated into pore-network models or used to provide parameters for the upscaling to reservoir scale [20]. X-ray Computed Microtomography (µCT) enables the characterisation of pore-scale displacement events and the quantification of key topological and geometrical parameters within the porous medium [21]. Timeresolved (4D) µCT provides particularly useful insights because it can capture dynamic fluid displacement processes. In addition, scans can be acquired without stopping fluid injection, thus avoiding the risk for fluid rearrangement induced by the injection pauses commonly employed in conventional (3D) µCT [22].

 μ CT-investigations of the H₂ distribution in sandstone are limited in number (Table 1). Initial saturations, S_{nwi} , in these studies span from 2 to 82 %, and residual saturations, S_{nwr} , vary between 0 and 45 %. Several studies suggests that heterogeneities and channels in the pore structure may cause substantial variability in the H₂ distribution in the pore space [25,30], leading to large variations in the S_{nwi} and S_{nwr} even for the same sandstone (Table 1). The role of pressure and temperature is less clear, yet current studies indicate that a higher pore fluid pressure, within the studied range of 1–10 MPa, does not increase the S_{nwi} (see Table 1 [13,16,26–28]). Comparison of μ CT-studies in Gosford sandstone suggests that a higher porosity causes higher S_{nwi} (Table 1; [23,24]).

In addition to visualization of the H_2 distribution in the pore space, a good understanding of the H_2 fluid flow during and after injection into the subsurface can be gained from characterization of the rock porosity, absolute permeability (Kr), pore network connectivity, tortuosity, and the determination of relative permeability/capillary pressure relationships with varying fluid saturation [26,33]. To date, relative permeability, kr, investigations of H_2 /brine/rock systems are restricted to six studies. Studies employing the steady state methodology [28,30–32,34] generally report low H_2 end-point kr of ≤ 0.1 (Fig. 1).

Real-time imaging of H_2 saturation and connectivity, linked to relative permeability, provides valuable insights into H_2 fluid flow behaviour in a given porous medium. In this work time-resolved synchrotron X-ray computed microtomography and radiography was employed to visualize H_2 and brine flow in Clashach sandstone, achieving a temporal resolution of 20 seconds/900 projections and an image resolution of $7.9~\mu m^3$. No blurred fluid interfaces were observed in the images, implying that the temporal resolution was sufficient to capture the important dynamics. Recognizing that there are pores below the image resolution, the focus of this work is on H_2 , which, being the non-wetting phase, occupies the largest pores in the rock. At the time of writing, no other time-resolved study of H_2 displacement in rock has been published.

We analysed the evolution of the H_2 saturation in relation to the connectivity of the H_2 fluid phase (via the use of the Euler characteristic, χ), in order to understand its controls on the H_2 saturation in the pore space. Hydrogen saturations at different H_2 to brine injection ratios are summarized in a fractional flow graph which allows the estimation of a set of L, E and T empirical fitting parameters for the H_2 brine relative permeability (where L influences the lower part of the curve, T influences the top part, and E influences the elevation or the positions of

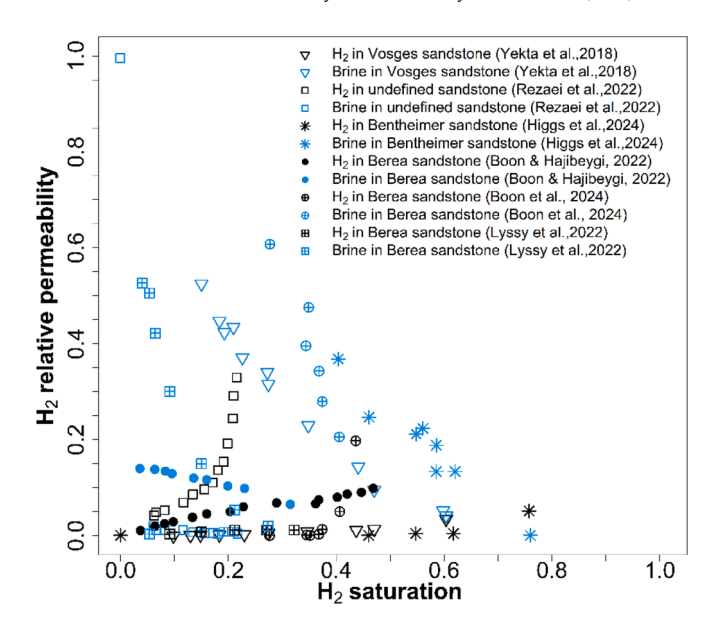


Fig. 1. Drainage relative permeability for the hydrogen-water system as investigated by previous studies, in which the relative permeability is calculated from the production data for gas and water, and the pressure difference and flow. With exception to the study by Rezaei et al. [17], all studies used the steady state technique.

the slope [35]). The results show similar H_2 connectivity at a H_2 fractional flow of 0.5 and 0.75. Hydrogen saturation increased by 5–8 % at the higher H_2 fractional flow. Our observations indicate displacement by means of Haines jumps and show intermittent flow in parts of the rock. The presented data may serve to improve pore-scale and reservoir models for appropriate understanding of gas storage operations.

2. Materials and methods

2.1. Core-flooding experiments

We performed two-phase unsteady state and steady state core flooding experiments with H₂ (purity 99.9995 vol%, BOC Ltd.) and brine (2 M KI, Sigma-Aldrich) in a Clashach sandstone sample. The Clashach sandstone is a Permian aeolian sandstone sourced from near Elgin, Scotland, characterised by a composition of 72.4 wt% quartz, 10.3 %albite, 6.2 % microcline, 2.7 % illite, 1.6 % kaolinite, 1.6 % orthoclase, 1.2 % corundum, 0.7 % calcite, 0.4 % chlorite and 0.2 % gypsum [10], and a porosity ranging from 12-18 % [36]. Experiments were performed at ambient temperature (~293 K) and a pore fluid pressure of 5 MPa. Fluid distributions and rearrangements within the sample were captured using synchrotron X-ray radiation (Diamond Light Source, I12-JEEP beamline). The experimental setup was as detailed in Thaysen et al. [13] (see SI Fig. S1). In summary, the Clashach outcrop sample, measuring 4.7 mm in diameter and 54 mm in length, was cleaned ultrasonically in acetone before undergoing H2 and brine injections. Experiments used four high-pressure pumps (Cetoni NemesysTM): Two pumps were operated at constant flow, one delivering H2 to the inlet of the rock sample, the other brine. A third pump, operating as a receiver at a constant pressure of 5 MPa, was connected to the production face of the sample. The fourth pump held a constant confining pressure of 10 MPa. Steady state injections used a total flowrate, q, of 20 μ l/min and were conducted with H₂ and brine flow rates of 10 μl/min each (ratio 1:1) and 16 μ l/min H₂ with 4 μ l/min brine (ratio 4:1), respectively. The first experiment injected H2 and non-H2-equilibrated brine simultaneously at a ratio of 1:1 into the brine-saturated rock sample, then the flow rates were changed to achieve a H2:brine ratio of 4:1 (the sample was not re-saturated with brine between experiments). During steady

state injections, the differential pressure across the sample was logged every 5 seconds using cross-calibrated ESI Technology GS4200 0–10 MPa pressure transducers with 0.1 % full-scale accuracy (Fig. 2). Bulk capillary numbers (N_c), which measure the balance between viscous and capillary forces, were calculated for H₂ fractional flows of 0.5 (ratio 1:1) and 0.75 (ratio 4:1) according to Eqs. (1) and (2), yielding values of 4.73 \times 10⁻⁹ and 2.97 \times 10⁻⁹, respectively.

$$Nc = \frac{q}{\lambda \sigma} \tag{1}$$

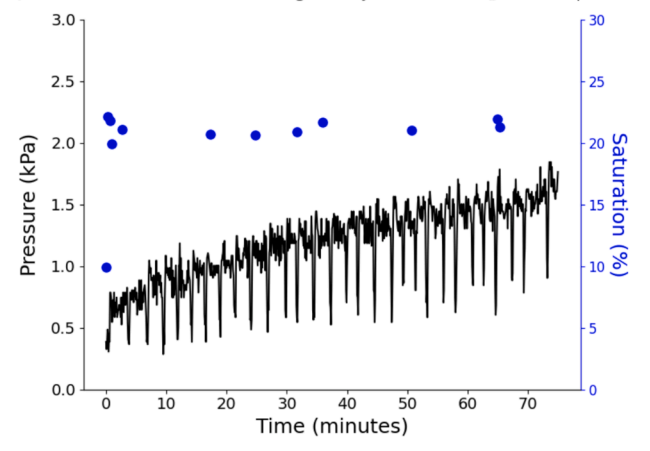
$$\lambda = \frac{f_w}{\mu_w} + \frac{1 - f_w}{\mu_g} \tag{2}$$

where σ is the interfacial tension between H₂ and water of 72.6 mN m⁻¹ (298 K and 5 MPa [37,38]), λ is the mobility ratio, defined in Spurin et al. [39], f_W is the fractional flow of the brine, μ_g is the viscosity of H₂, of 9.01 μ Pa s (at 298 K and 4.7 MPa [40]), and μ_W is the viscosity of the brine of 1.07 \times 10⁻³ Pa s (0.6 M KI and 293 K [41]). Unsteady state injections of H₂ into a brine saturated rock (drainage) used a flowrate of 5 μ l min⁻¹, corresponding to a N_c of 4.3 \times 10⁻⁹.

Time-resolved 3D tomographic scans were acquired to record the evolution in $\rm H_2$ saturation and connectivity over time. To capture dynamic fluid processes that occur over timescales that are faster than a single time-resolved 3D scan (i.e. <20 seconds), 2D radiographs were acquired. While losing the volumetric information offered by tomographic volumes, 2D radiographs enabled the visualisation of processes occurring over timescales of 10 s to 100 s of milliseconds.

For steady state injections, time-resolved (4D) tomographic imaging

a) Pressure and saturation during 1:1 injection ratio H₂/brine experiment



b) Pressure and saturation during 4:1 injection ratio H₂/brine experiment

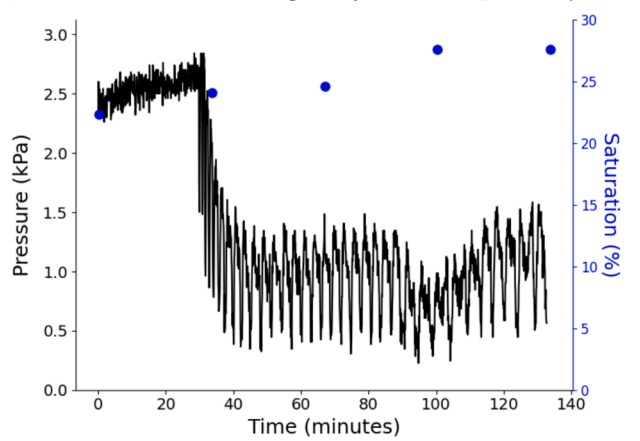


Fig. 2. Differential pressure vs time in steady state injections of H_2 and brine at a) an injection ratio of 1:1 H_2 /brine and b) an injection ratio of 4:1 H_2 /brine.

of the $\rm H_2$ and brine displacement processes was achieved by means of a 65 keV monochromatic beam with a bandwidth of 2×10^{-3} and the beamline's scintillator-coupled Pioneering in Cameras and Optoelectronics (PCO) edge 5.5 imaging camera ('Module 2' with a 7.91 \times 7.91 $\mu m/pixel$ size and a field of view of 20 mm \times 12 mm - see [42]). A total of 900 projections with 20 seconds exposure time were recorded for each time-resolved μCT scan. The voxel size was 7.9 μm^3 . Scans were acquired sequentially using a sequence of clockwise then anticlockwise 180° half-rotations to enable near-continuous (non-stop) scanning.

Unsteady state injections were captured using live 2D radiography with a 25-millisecond exposure time per frame and 900 frames per acquisition, with consecutive acquisitions running for 78 min.

2D radiographs and 3D projections were acquired from the lower central portion of the sample to avoid the impact of capillary end effects on fluid saturation, where the wetting phase accumulates close to the production face of the core [43,44]. Despite being considered a serious source of error [43], capillary end effects have been neglected in many previous H₂ fluid flow studies (e.g. [23,25,28,45]).

2.2. Image analysis

2.2.1. Time-resolved (4D) µCT scans

Tomographic reconstructions were undertaken by filtered back projection using Octopus 8.9 [46] on a GPU accelerated workstation. To accurately segment the various phases (H_2 , brine, and rock) in the reconstructed projections we modified the workflow outlined in Rizzo et al. [47]:

Manual labelling of phases in a subset of three horizontal (XY) slices (out of the 2150 total slices composing each tomogram) using the brush tool in Dragonfly (Comet Technologies, Canada).

Running a random forest classifier on the labelled data, incorporating morphological, Gaussian multi-scale, and neighbour-based features, to label all pixels in the three slices. The fully labelled slices represent the ground-truth dataset.

Manually correcting the slices labelled by the random forest classifier.

Applying a 2.5D U-net deep-learning algorithm in the slow and better mode and a 80–20 % split of the manually corrected slices as training and validation datasets.

The trained model was then deployed on all time-resolved scans where successful segmentation of all three phases was accomplished in approximately 1 hour per volume (2150 slices/phase, $\sim 7.24~\mathrm{GB}$ each), utilizing a workstation equipped with 128 GB of RAM, an Intel Xeon W-2125 CPU processor, and a 11 GB NVIDIA GeForce RTX 2080 Ti GPU with 11 GB of RAM and 4352 CUDA cores.

The sample porosity was computed in Dragonfly using a scan of H_2 injection into a dry rock. After the segmentation, all subsequent image processing and analysis was performed by applying our established workflow [13] in Avizo Version 9.1.1 (FEI, Oregon, USA) on a representative subvolume of the total scanned section of the rock sample. The subvolume (900 \times 1000 \times 800 $\mu m)$ was defined based on the porosity fraction of the rock, and had a porosity which matched the total porosity of the rock closely (13.3 % vs. 13.6 % porosity, respectively). Because the whole rock volume contained zones into which H_2 never entered (SI Fig. S2 and S3), the subvolume was also selected in terms of a representative H_2 saturation and connectivity. Image processing after segmentation used a spot filter for features which were at the resolution limit of the data (the applied threshold corresponded to 5^3 voxels).

In scans acquired following brine and H_2 injections, the segmented H_2 volume was analysed using the Avizo 'labelling' and 'label analysis' modules to identify, label and measure the volume of each H_2 ganglion, and to quantify its connectivity (via the Euler characteristic, χ). Application of this metric allows tracking of the connectivity evolution with variations in injection rates, a valuable insight for predictive modelling

in heterogeneous reservoirs.

The Euler characteristic is a topological invariant (as opposed to shape which changes with bending and stretching) and for a 3D object it is defined as:

$$\chi = \beta_0 - \beta_1 + \beta_2 \tag{3}$$

where β_0 , β_1 and β_2 are Betti numbers zero, one and two, respectively. The zeroth Betti number refers to the number of distinct elements of fluid in the volume, the first Betti number refers to the number of handles or redundant loops present in the structure of each fluid component, while the second Betti number indicates the number of enclosed voids in the fluid component. A highly connected phase has a large negative χ , and a highly disconnected phase has a large positive χ [48]. An average Euler characteristic, $\mu\chi$, was calculated for the entire subvolume.

2.2.2. Live radiography (Time-resolved 2D X-ray imaging)

Enhancement of the radiographs and video was performed using Fiji-ImageJ [49], following subsequent steps:

- 1. Flat and dark field correction of raw images
 - a. Average dark and flat field images were generated from the multiple flats and darks provided.
 - b. Flat and dark field images were cropped to the size of the live radiography video using specks as marker points.
 - c. Correction of the radiographs was applied as:

$$R_{c} = \frac{(R_{r} - D)\overline{(F - D)}}{(F - D)} \tag{4}$$

where R_c and R_r are the corrected and raw radiographs, respectively, and F and D are the flat and dark field images, in each case.

- Fiji's Integral Image Filter Remove Outliers tool was used to despeckle the corrected radiographs (block radius x = 40, block radius y = 40, standard deviations = 3.00).
- $3. \ \,$ The corrected radiographs were cropped to remove the background.
- 4. Contrast-limited adaptive histogram equalisation (CLAHE) was applied to each radiograph (block size = 127, histogram bins = 256, maximum slope = 2).
- 5. A non-local means filter (sigma = 2200, factor = 2) and a median filter (sigma = 1) were applied.
- 6. After contrast re-scaling (using 14,200–41,000 as the new 16-bit min–max), the video was saved in slow motion starting from frame 351 at 10 frames/second with JPG compression, equating to a time difference of +75 milliseconds between the slow-motion video and the real time. The real time duration of the video would be 13.8 seconds, considering an exposure time of 0.025 seconds per frame, and 550 frames.

2.3. Absolute permeability estimations using unsteady state injection experiments

The absolute permeability, Kr, was estimated using Darcy's Law method according to Eq. (5) from unsteady state injections of brine into the Clashach sandstone sample.

$$Kr = \frac{\mu \ LQ_0}{A_0 \Delta P} \tag{5}$$

where μ is the dynamic viscosity of the brine, L is the length of the sample, Q_0 is the volumetric flow rate calculated by integrating the sample output, A_0 is the cross-sectional area of the cylindrical sample and ΔP is the pressure gradient across the core.

2.4. Relative permeability estimations using steady state injection experiments

The $\rm H_2$ relative permeability was estimated by adopting the workflow outlined in Krevor et al. [50] by fitting the LET model [35] to the fractional flow, f, and $\rm H_2$ saturation data in the whole rock volumes acquired in this work and in Thaysen et al. [13] (see SI Fig. S2-S3 and S4respectively). The fractional flow graph, which illustrates the relationship between the flow rates of each phase, constrains the ratio of the relative permeabilities, specifically

$$f_{w} = \frac{1}{\left[1 + \left(\frac{\mu_{w}}{\mu_{H2}}\right)\left(\frac{kr_{H2}}{kr_{w}}\right)\right]} \tag{6}$$

where kr is the relative permeability-saturation relationship and the subscripts w and H_2 refer to water and hydrogen, respectively [50]. The LET relations for relative permeability for water and H_2 are given in Eqs. (7)–(9) [35]:

$$k_{rw} = \frac{Kr_w S_{wn}^{Lw}}{S_{wn}^{Lw} + E_w (1 - S_{wn})^{Tw}}$$
(7)

$$k_{rH2} = \frac{Kr_{H2}(1 - S_{wn})^{LH2}}{(1 - S_{wn})^{LH2} + E_{H2}(S_{wn}^{TH2})}$$
(8)

$$S_{wn} = \frac{S_w - S_{wi}}{1 - S_{wi}} \tag{9}$$

where the absolute permeability, Kr, has a value of 1 and the variables L, E and T are used as empirical fitting parameters, with L influencing the lower part of the curve, T influencing the top part, and E influencing the elevation or the positions of the slope. S_w and S_{wi} are the water saturation and the irreducible water saturation, respectively. S_{wn} , calculated by Eq. (9), is the normalized water saturation. The S_{wi} for Clashach sandstone is 12.6–14.0 % [18] and was set to 13.3 % in the relative permeability simulations.

3. Results

3.1. Segmentation

The uCT grevscale slices exhibited high phase contrast, manifested as white rims around pore edges and grey levels within the black hydrogen bubbles (Fig. 3a). While this contrast aided in visually distinguishing the H₂, brine, and rock phases, it posed challenges for classical segmentation approaches due to overlapping greyscale values across phases (Fig. 3b). Hence, we applied a deep learning segmentation which is not solely based on greyscale thresholds but is also sensitive to the geometry of distinct phases. The optimized deep-learning segmentation model had a DICE coefficient [51] of 0.87 for the hydrogen phase of the validation data set (SI Fig. S5), indicating high similarity between predicted and ground truth slices. Yet the model slightly overestimated the H2 volume by including portions of the white rims (Fig. 3c). However, erosion of the H₂ label by a single voxel led to underestimation (Fig. 3d), demonstrating the partial volume effect [52] and the difficulty in achieving perfect segmentation under these conditions. The change in the average Euler number associated to the erosion by 1 voxel was substantial (Fig. 3c and d) and was accompanied by a decrease of 31 % and 2 % in the mean size and total number of the H₂ ganglia, respectively, suggesting lots of narrow connections across the pore space for the gas and a high sensitivity of the Euler number to the image segmentation in our experiments.

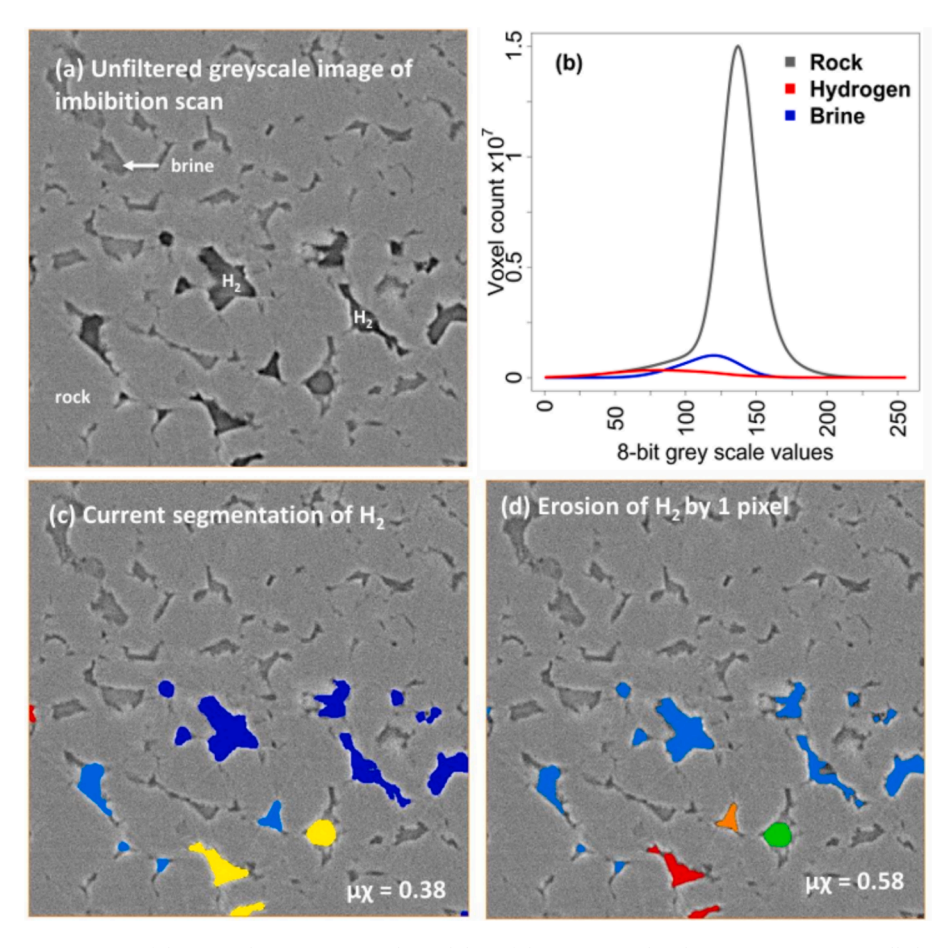


Fig. 3. Performance of the segmentation of the H_2 in the pore space and sensibility of the average Euler characteristic ($\mu\chi$) to small changes in labelled volume. (a) Greyscale image of imbibition with rock shown in light grey, brine in dark grey and hydrogen in black. (b) Histogram showing the range of grey scale values occupied by rock, brine and H_2 , respectively. (c) segmentation with $\mu\chi$ showing that the white rims around the pores (i.e. rock) are mostly but not entirely preserved. (d) Segmentation eroded by one voxel showing that the white rims are entirely preserved but the volume of H_2 is not entirely labelled.

3.2. Evolution of H_2 saturation and connectivity in steady state injection experiments

In this section we evaluate the H_2 distribution and connectivity in the pore space as a function of time. A qualitative evaluation is achieved by isolating H_2 clusters from segmented slices and giving each cluster a distinct colour (Figs. 4 and 5, SI Fig. S2 and S3). The quantitative assessment of the fluid connectivity is based on the Euler characteristic, χ (see methodology), where a large negative χ is indicative of a highly connected phase, and a large positive χ represents a highly disconnected phase [48].

During steady state injection of H_2 and brine at a ratio of 1:1 into a brine-saturated rock, the H_2 initially occupied only a small portion of the pore space within the subvolume, with numerous small and poorly connected clusters (9.9 % H_2 saturation, average Euler number $\mu\chi=0.7$ at t=0; Fig. 4, and Fig. 6a, pale green curve where the frequency was divided by 4). The largest H_2 cluster at this stage measured 0.22×10^7 μm^3 (Fig. 6a and c, respectively). Across the total visualized rock volume, the gas saturation was higher (15 %) but connectivity remained uneven (SI Fig. S2). For instance, the upper section of the column contained a single large, connected ganglion of H_2 , while the lower section showed several disconnected H_2 ganglia (SI Fig. S2). Within just 0.3 min, the H_2 saturation rose to 22 % (Fig. 4). At this point, most of the H_2 was concentrated in a single, well-connected cluster, resulting in a significantly lower Euler characteristic ($\mu\chi=-1.5$; Fig. 4). The size of this dominant H_2 cluster was 2.3×10^7 μm^3 (Fig. 6a and c).

In subsequent scans, corresponding to 0.67-65.3 min after gas arrival in the visible region of the rock sample, the H_2 saturation

stabilized between 20–22 % with $\mu\chi$ fluctuating between -0.1 to 0.6, suggesting a weakly connected gas phase (Fig. 4). The amount of H_2 fluctuating between scans during this steady state, as determined via subtractions of one subvolume from the other, was 10 %. The cluster size distributions during this period showed cumulative volumes that remained almost constant, ranging from ~ 1.9 to 2.3×10^7 μm^3 (Fig. 6c). However, the shape of the cluster size distribution evolved over time, with an increasing number of intermediate-size clusters observed between 2.7 and 65.3 min compared to the earlier stage (2–3 min; Fig. 6a). This shift brought the cluster distribution closer to the pore size distribution (PS, black stippled line, Fig. 6a). These changes in the arrangement of H_2 were not immediately apparent from visual inspection of the μ CT images (Fig. 4).

At any time, the largest $\rm H_2$ clusters spanned multiple pores, consistently exceeding the maximum volume of discrete pores of 1.3×10^6 μm^3 (Fig. 6a; black stippled line for PS/20): nevertheless they were always smaller than the largest cluster observed during 100 % $\rm H_2$ injection into Clashach sandstone in prior studies [13]. The trends in $\rm H_2$ saturation and connectivity observed in the whole rock volume mirrored those seen in the subvolume (SI Fig. S2 and S3).

During steady state injection at a H_2 fractional flow of 0.75 into a rock sample that had been initially saturated with fluid corresponding to a H_2 fractional flow of 0.5, the H_2 saturation in the pore space increased from 22 % at time $t_0+0.3$ min to 24–25 % at $t_0+33.7$ and t_0+67 min after gas arrival in the field of view of the column (Fig. 5). By $t_0+100.3$ min, the H_2 saturation reached 27.6 % and remained unchanged at 133.7 min (Fig. 5). The $\mu\chi$ remained relatively stable at approximately 0.6 for scans at 0.3, 33.7 and 67 min, before decreasing to \sim 0.3–0.4 at

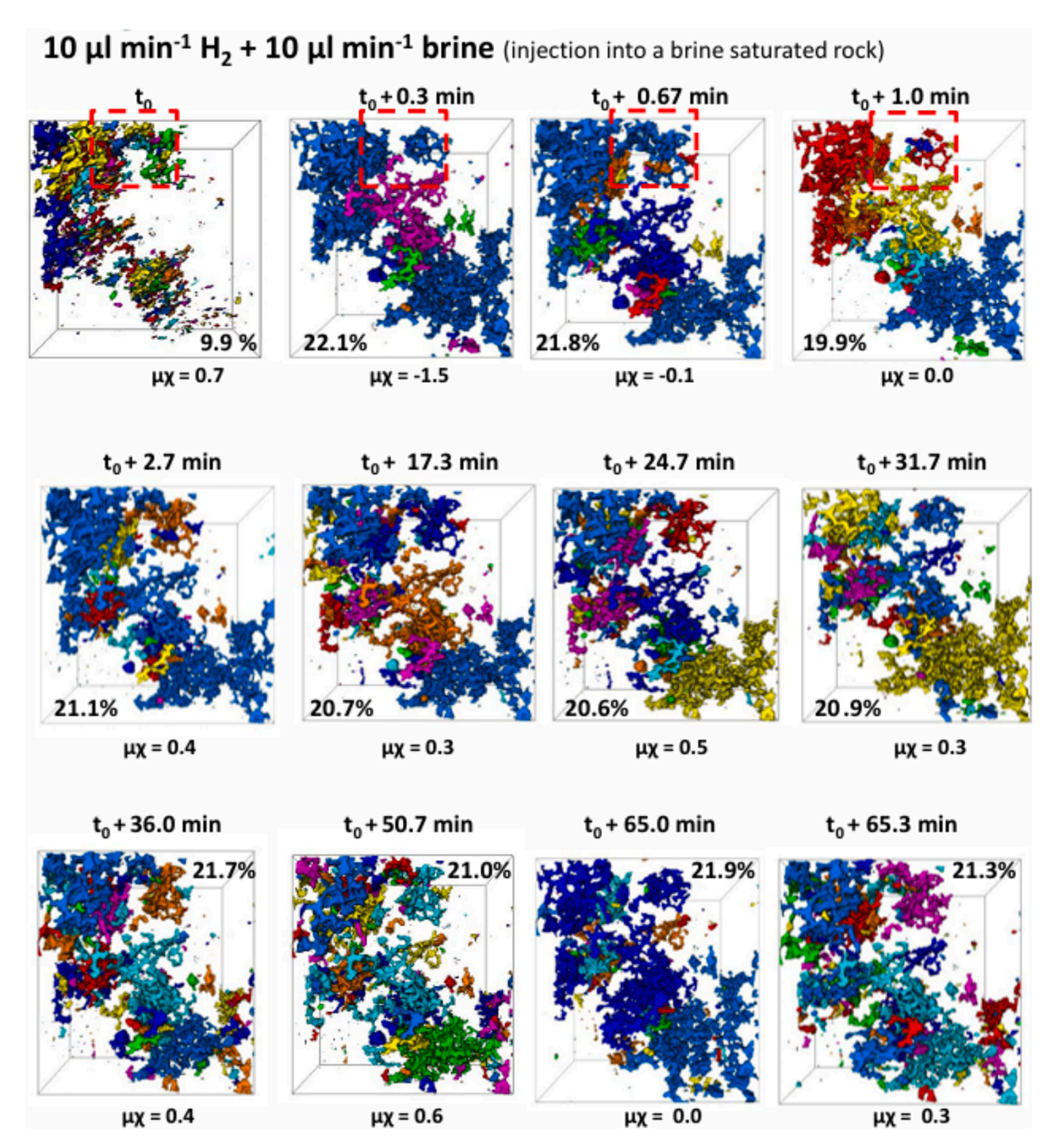


Fig. 4. Hydrogen saturation and connectivity as a function of time in a subvolume of the pore space in steady state injection experiments at 5 MPa and $10 \,\mu l$ min⁻¹ H₂ plus $10 \,\mu l$ min⁻¹ brine. The 3D volume of the boxes is 356.3 mm³ and the vertical edges of the boxes measure 7.1 mm. Colours distinguish disconnected H₂ clusters, with large, uniformly coloured areas representing connected ganglia, indicating variations in phase connectivity. Percentages in the corners of the graphs indicate the H₂ saturation. $\mu \chi = average$ Euler characteristic. The red square at times t_0 to $t_0 + 1$ min shows where intermittent H₂ flow is observed.

100.3–133.7 min (Fig. 5). Hydrogen clusters followed a normal distribution that was of similar shape as the pore size distribution, and the shape of the distribution did not change significantly over time (Fig. 6b). However, the size of the largest $\rm H_2$ cluster increased over time from 2.0–2.6 \times $10^6~\mu m^3$ at 33.7 and 67 min to 6.4–9.8 \times $10^6~\mu m^3$ at 100.3–133.7 min (Fig. 6b), corresponding to an increase from 1.9–2.5 % to 6.2–9.5 % in pore space occupancy, respectively. At all times, the largest $\rm H_2$ clusters were larger than discrete pores with a maximum volume of 1.3 \times $10^6~\mu m^3$ and a mean volume of 3.1 \times $10^4~\mu m^3$ (Fig. 6b). The cumulative $\rm H_2$ volume in the pore space increased from 2.2–2.5 \times $10^7~\mu m^3$ at 0.3 and 33.7 min to 2.8–2.9 \times $10^7~\mu m^3$ at 67, 100.3 and 133.7 min (Fig. 6d), and was hence significantly higher than for the $\rm H_2$

fractional flow of 0.5. Notably, there was no identifiable H_2 phase ingress into specific zones within the rock sample, regardless of the H_2 fractional flow (SI Fig. S2 and S3; upper right part of the rock).

3.3. H_2 filling of the pore space

Fig. 7 shows a close up view of H_2 entering a small subvolume of the pore space during steady state injections of H_2 into a brine saturated rock at a H_2 fractional flow fraction of 0.5. Sequential scans reveal how clusters disconnect and reconnect over time, demonstrating intermittent flow patterns: Upon gas arrival in the subvolume, H_2 fills merely a couple of pores (Fig. 7a). Within 20 seconds, H_2 enters a new space

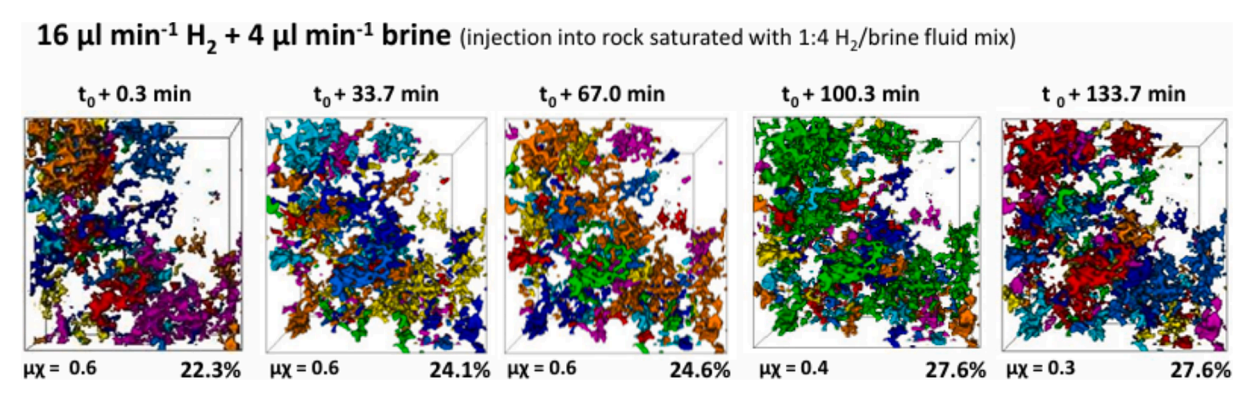


Fig. 5. Hydrogen saturation and connectivity as a function of time in a subvolume of the pore space in steady state injection experiments at 5 MPa 16 μ l min⁻¹ H₂ plus 4 μ l min⁻¹ brine. The 3D volume of the boxes is 356.3 mm³ and their vertical edges of the boxes measure 7.1 mm Colours distinguish disconnected H₂ clusters, with large, uniformly coloured areas representing connected ganglia, indicating variations in phase connectivity. Percentages below the graphs indicate the H₂ saturation. $\mu\chi$ = average Euler characteristic.

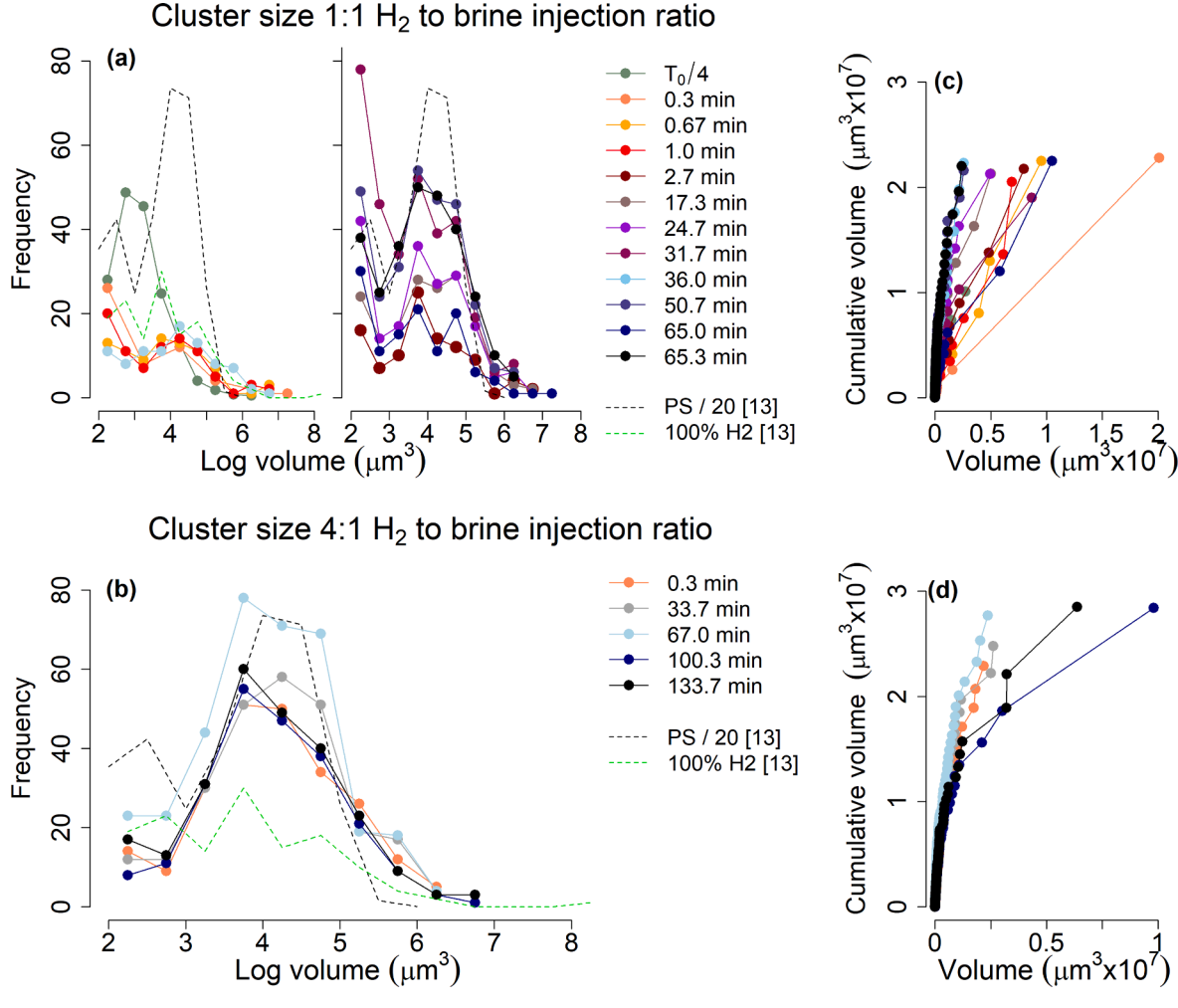


Fig. 6. Hydrogen cluster size distributions as a function of time at steady state injections of (a) $10 \,\mu l \,min^{-1} \,H_2 \,plus \, 10 \,\mu l \,min^{-1} \,brine$, and (b) $16 \,\mu l \,min^{-1} \,H_2 \,plus \, 4 \,\mu l \,min^{-1} \,brine$, together with the pore size distribution of Clashach sandstone with the frequency divided by 20 (PS/20, black stippled line), and the drainage curve for $10 \,PV$ of H_2 injected at 5 MPa and $20 \,\mu l \,min^{-1}$ (green stippled line; both from Thaysen et al. [13]). (c) and (d): cumulative hydrogen cluster size distributions at $10 \,\mu l \,min^{-1} \,H_2 \,plus \, 10 \,\mu l \,min^{-1} \,brine$, and $16 \,\mu l \,min^{-1} \,H_2 \,plus \, 4 \,\mu l \,min^{-1} \,brine$, respectively. Note the different x-axes in (c) and (d), and that the frequency was divided by 4 for the t_0 data in (a) and (c).

extending over several geometrically defined pores, and expansion of the H_2 -filled pore space into the subvolume is from different sides (Fig. 7a, b). At the same time, some H_2 clusters are broken up (upper left corner in Fig. 7b). At $t_0 + 40$ s the majority of the H_2 in the lower part of

the subvolume is displaced by brine and H_2 clusters that were snapped off at t_0+20 s reconnect (Fig. 7c). Another scan later, at time t_0+60 s, H_2 occupies almost the same pores as at t_0+20 s (Fig. 7d, b). Transient H_2 pore occupancy was also observed on a larger scale (Fig. 4, red

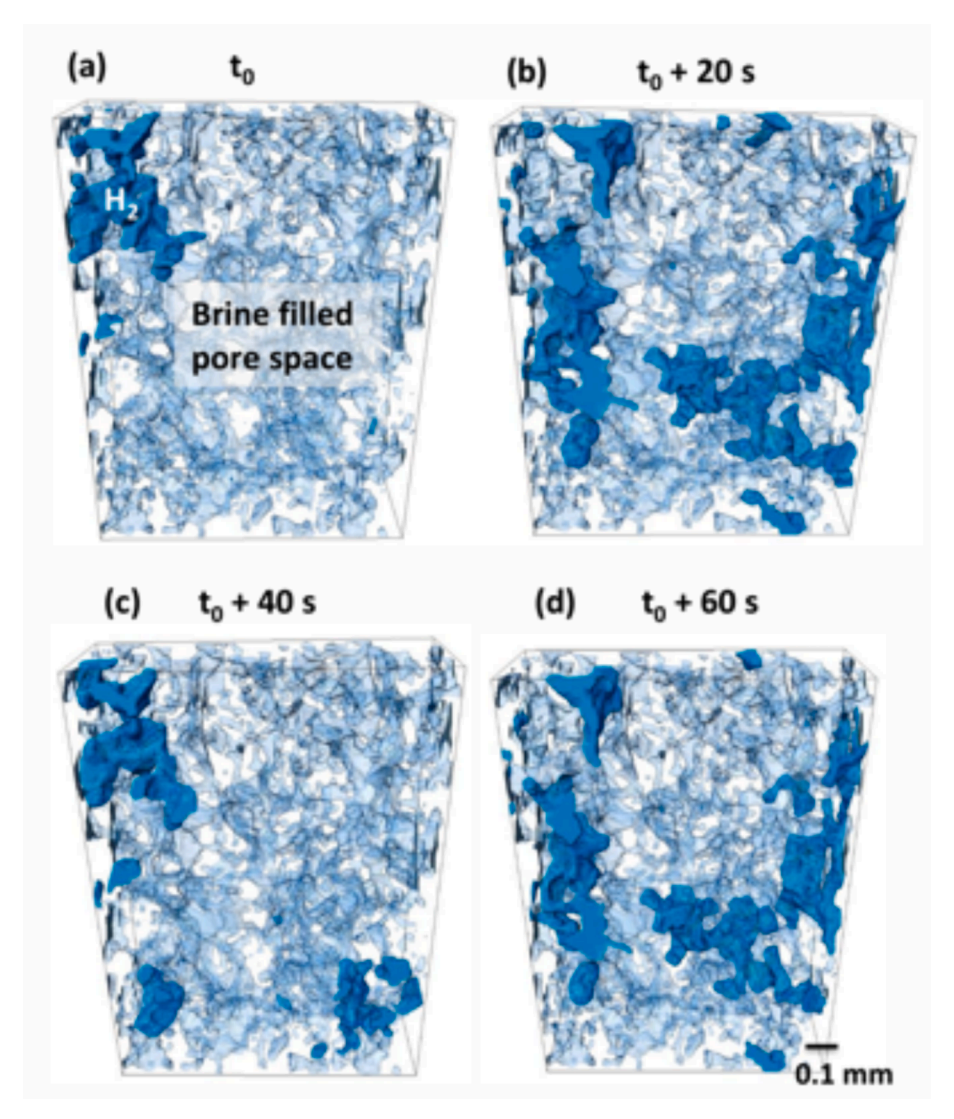


Fig. 7. Time-lapse series of steady state injections of H_2 and brine into a brine saturated Clashach sandstone sample, at flow rates of $10 \mu min^{-1}$ for both H_2 and brine. (a) + (b): Over a 20 second time interval, H_2 (royal blue) fills multiple pores (transparent blue), entering the subvolume of 6.6 mm³ from different sides. At the same time, some gas clusters are snapped off (upper left corner in (b) vs (a)). (c) and (d): H_2 moves back to occupy nearly the same pores as in (a) and (b), respectively.

squares).

Two-dimensional static radiography scans of the drainage process (unsteady state injections) show that H_2 enters the rock within seconds, filling multiple pores at once in a discontinuous, sudden manner (Fig. 8/supplementary video file).

3.4. Pressure fluctuations during steady state injections

By transforming the pressure data into the frequency domain using a continuous wavelet transformation and the methodology described in [53], we can explore how events evolve with time. The spectral power with time is shown in Fig. 9. At both the $\rm H_2$ fractional flow fractions of 0.5 and 0.75, the pressure oscillations had intervals of 2–3 min (Fig. 9b and d; this equates to a frequency of 10^{-2} Hz). Both injection schemes can be classified by red noise (a slope of –2 in the log–log space, as shown by the red dashed lines in Fig. 9b and d). This means that larger amplitudes have longer periods. This was observed for intermittent pathway flow, where larger events (in terms of volume of fluid involved) occurred less regularly [39]. The pressure signal prior to gas arrival was characterized by white noise (random noise for frequencies > 10^{-3} Hz; SI Fig. S6).

3.5. Relative and absolute permeability estimations

Fig. 10a shows the fractional flow versus saturation curve for the Clashach sandstone in current experiments and in experiments in Thaysen et al. [13], as well as the best-fit model parameters produced from the LET relative permeability curves (Eqs. (7)–(9); Fig. 10b). Hydrogen saturations increase with increasing $\rm H_2$ flow fraction but remain relatively low even at a fraction of 1 (max. ~ 50 % saturation). The absolute permeability of the Clashach sandstone sample was calculated to 35 mD.

4. Discussion

4.1. Evolution of H_2 saturation and connectivity in steady state injection experiments

The H_2 saturation in the pore space increased by 6-8% with an increase in the H_2 fractional flow from 0.5 to 0.75 (Figs. 4 and 5, SI Fig. S2 and S3), in line with previous experiments by Thaysen et al. [13] (SI Fig. S4). This implies that for H_2 storage into sandstone aquifers with injection-induced hydrodynamic flow, the amount of H_2 that can be

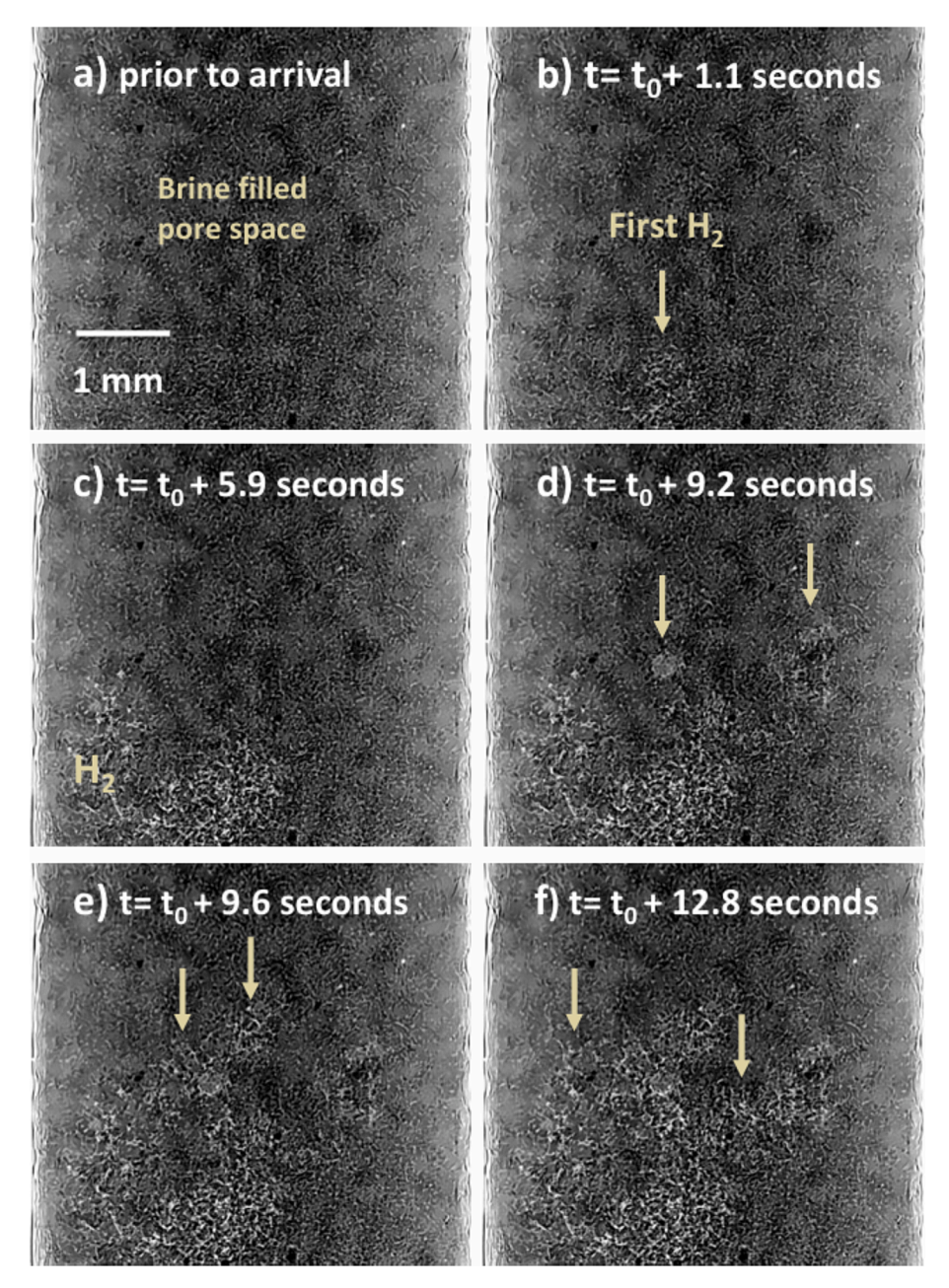


Fig. 8. linking to the video in the supplementary information: 2D-imaging of H₂ entering the brine saturated Clashach sandstone sample at a flow rate of 5 μ l min⁻¹, corresponding to $Nc = 4.25 \times 10^{-9}$. Hydrogen moves in bursts, filling multiple pores at once (see arrows).

injected decreases with increasing flow. At both H_2 flow fractions, the $\mu\chi$ was generally positive (Figs. 4 and 5), indicating poor connectivity of the H_2 gas. While a slight decrease in $\mu\chi$ with increasing H_2 saturation was observed in the 4:1 flow fraction experiment (Fig. 5), in the 1:1 flow fraction experiment the $\mu\chi$ varied without clear trend despite constant H_2 saturation (Fig. 4). This suggests little control of phase connectivity on H_2 saturation. However, it is important to note that the Euler measure is sensitive to the resolution of μ CT projections [54]. The Clashach sandstone holds a large amount of pores with radius <5 μ m [13]. Hence a voxel size of the μ CT projections of only 7.9 μ m³ is likely to cause some underestimation of the true H_2 connectivity (i.e. the actual $\mu\chi$ is likely less positive) [54]. Being the non-wetting phase though H_2 preferentially enters bigger pores [13].

Changes in phase connectivity at constant saturation have been shown previously for oil and brine two phase flow but in relation to increases in N_C [55]. While the bulk N_C was constant in the 1:1 flow fraction experiment, variations in the local N_C may have prompted

variations in the $\mu\chi$. The $\mu\chi$ was not higher at the higher fractional flow of H₂ at similar points in time (Figs. 4, 5). This weak connectivity of H₂ ganglia regardless of H₂ flow fraction suggests a generally low H₂ recovery from sandstone aquifers with injection-induced hydrodynamic flow. In aquifers with naturally occurring or farmed H₂ the brine flow will be much lower (no injection-induced flow) which is likely to have a positive effect on H₂ connectivity and recovery.

Previous steady state experiments with H_2 and brine [13] showed increased H_2 connectivity with fractional flow (SI Fig. S4, based on visual assessment). However, here projections were captured after injection was stopped which may have rearranged or fused some of the H_2 clusters [26]. Since the scans for previous steady state experiments showed no evidence of fluid rearrangement during tomographic data acquisition (1-hour scans; rearrangement manifests as blurry pores) nor during a 10-hour lock-in period after injection stop [13], rearrangement or fusing would need to have occurred in the timespan between ceasing the delivery of H_2 and the start of the scan.

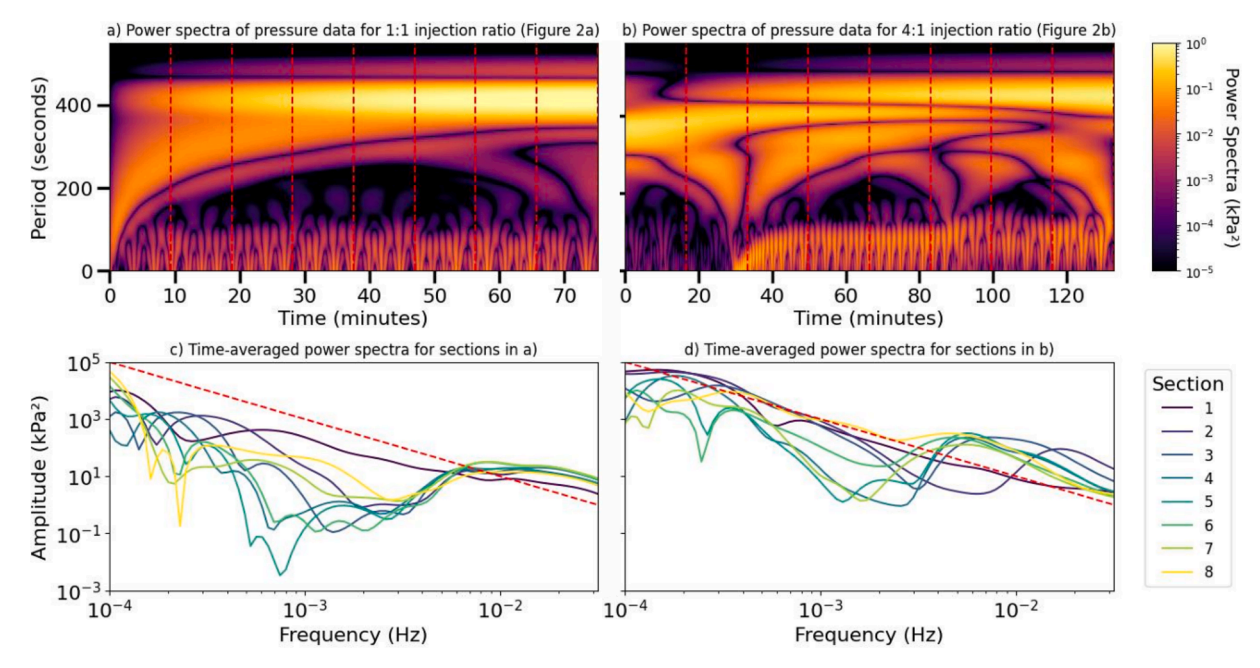
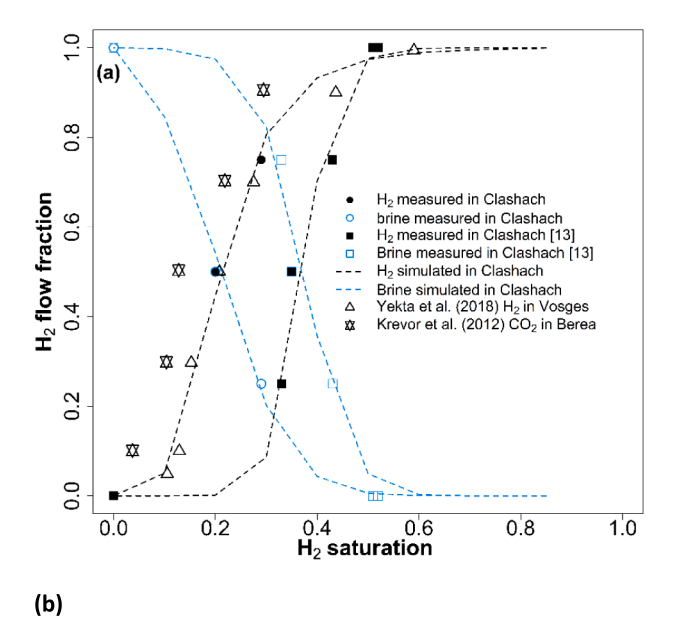


Fig. 9. Power spectra calculated by transforming the pressure data in Fig. 2 for the $10 \,\mu l$ min⁻¹ H_2 plus $10 \,\mu l$ min⁻¹ brine injection (a) and the $16 \,\mu l$ min⁻¹ H_2 plus $4 \,\mu l$ min⁻¹ brine injection (b). c) and d): Time-averaged power spectra of the $10 \,\mu l$ min⁻¹ H_2 plus $10 \,\mu l$ min⁻¹ brine injection and the $16 \,\mu l$ min⁻¹ H_2 plus $4 \,\mu l$ min⁻¹ brine injection, respectively, with the sections averaged over indicated by the dashed lines in a) and b). The graticule for red noise is highlighted for comparison to previous work (red stippled line).



 T_{H2}

0.6

Parameter This work Thaysen et al. [13] Lysyy et al. [31] Clashach sandstone Clashach sandstone Berea Sandstone 7.5 (drainage); 7.5 (imbibition) 8.0 L_w 8.0 L_{H2} 3.8 8.5 1.6 (drainage); 4.2 (imbibition) E_w 0.25 0.06 2.95 (drainage); 2.0 (imbibition) 0.0055 0.007 6.0 (drainage); 2.5 (imbibition) E_{H2} T_w 0.6 2.0 0.52 (drainage); 0.6 (imbibition)

Fig. 10. (a) Hydrogen fractional flow versus hydrogen saturation for Clashach rock samples in this work and in Thaysen et al. [13], both at $20 \,\mu$ l min⁻¹ total flow rate corresponding to $Nc = 6.8 \times 10^{-8}$ for H_2 at $100 \,\%$ H_2 injection and $Nc = 2.4 \times 10^{-6}$ at $100 \,\%$ brine injection. The dashed lines are the plots based on best fit relative permeabilities calculated from the LET model. Data are compared to H_2 fractional flow data from Yekta et al. [34] for untreated Vosges sandstone at 5.5 MPa and $100 \,\%$ c, and to $100 \,\%$ fractional flow data from Krevor et al. [50] for untreated Berea sandstone at 9 MPa and $100 \,\%$ c. (b) Best fit $100 \,\%$ c and $100 \,\%$ model parameters for the hydrogen-water system in Clashach and Berea sandstone (all dimensionless).

0.9 (drainage); 0.6 (imbibition)

4.0

The observed lack of a significant connectivity increase (more negative $\mu\chi$) at higher H_2 fractional flow suggests that multiphase fluid flow, described by the relative permeability, is merely a function of pore space saturation, as often assumed [55]. Yet, changes in the $\mu\chi$ within the 1:1 flow fraction experiment where reflected by changes in pressure, while saturation remained more or less constant, indicating that connectivity does play a role in controlling the fluid flow. Previous 4D investigations of oil and brine injections at high N_C of 10^{-4} to 10^{-6} and a resolution of 4.2 μ m showed an important influence of phase connectivity, suggesting that χ should be considered along with the saturation to describe the two-phase fluid flow [55]. Future studies should investigate H_2 connectivity as a function of N_C at the highest possible resolution and increase the number of data points to clarify these possible impacts on our results.

At both $\rm H_2$ flow fractions, the cluster size distributions were not shifted to smaller or larger clusters (Fig. 6), indicating no wettability change during injection. In the 1:1 flow fraction experiment, the cumulative cluster size was almost constant throughout time but the pore occupation of $\rm H_2$ shifted towards smaller clusters beyond the scan at $\rm t_0$ + 0.3 min (Fig. 6c), suggesting that intermediate and smaller sized $\rm H_2$ clusters were controlling the difference between the scans.

4.2. Pore filling in steady state injection experiments

In the 1:1 flow fraction experiment, H₂ filled the brine filled pore space within seconds (Fig. 4, Fig. 7) to reach a relatively constant concentration of 20–22 % (Fig. 4) and constant cumulative volume (Fig. 6c), where, locally in the sample, H2 clusters connected to each other, disconnected from each other and then reconnected over time (Fig. 7). This phenomenon, recognized as intermittent pathway flow or simply intermittent flow, suggests that Darcy's law-which is widely used to describe multiphase fluid flow in porous media through relative permeability and capillary pressure and assumes that fluids flow in stable, connected pathways- may not adequately capture all of the H2 and brine flow behaviour. Intermittent flow was only evident in a small part of the larger subvolumes (Fig. 4, red squares), the large-scale H₂ distribution persisted with time (Fig. 4, SI Fig. S2). Combining this with the fact that the distribution of H2 clusters remained unchanged while the intermittent flow was observed (Fig. 7, Fig. 6a t0 to t0 + 1 min) and that the evolution of H2 saturation with H2 fractional flow could be described accurately using the conventional framework of relative permeability functions (Fig. 10a), suggests that intermittent flow was of more local nature in our experiments and that macro-scale flow properties such as the relative permeability were not affected. Our observations of a largely invariable H2 distribution combined with a continuously evolving H2 connectivity are consistent with previous research conducted with N2 and brine, where intermittent pathways were compared to cars controlled by traffic lights, with the overall network of flow pathways remaining constant [56].

Intermittent flow has been observed previously [55,57–60], also in N_2 steady state experiments, at N_c ranging from 4.54×10^{-8} to 1×10^{-4} [55–61]. To our best knowledge intermittent flow has never been reported at N_c as low as 4.7×10^{-9} . The fraction of intermittent flow to connected pathway flow increases with increasing N_c [61,62], increasing inertial forces over viscous forces in the flow (Reynolds number) [61] and decreasing viscosity ratio, M, which is ratio of the viscosity of the displaced fluid over the viscosity of the injected phase [62]. At low N_c , generally characteristic for subsurface conditions, and M > 1, connected pathways exist [62] and the location of any intermittency in the flow will be controlled by the pore geometry [61]. In our experiments, the N_c was low ($<10^{-8}$), suppressing intermittent pathway flow, but M was also well below 1 (8.4×10^{-3}) and much lower than in previous studies on N_2 (0.14–31 [56,62]) and oils (1–200 [62,63]), encouraging intermittency [62].

At higher N_c , intermittent H_2 transport can be expected to increase in magnitude, as shown previously for N_2 , where N_c of $0.38-1.1 \times 10^{-6}$

caused an increase in intermittent flow and a shift in the relative permeability curve [62]. Considering the lower M of the H_2 -brine system compared to the N_2 -brine system, relatively more intermittent flow can be expected for a given flow rate and shifts in the kr_{H2} can be expected at lower N_c than for N_2 . Future experiments should investigate the volume of intermittent H_2 flow as a function of N_c and fractional flow.

4.3. Pore filling in unsteady state experiments

Hydrogen displacement of brine during drainage occurred in rapid, discontinuous bursts that filled multiple individual pores in short time frames (Fig. 8/supplementary video file) and may be consistent with Haines jumps. In order to provide further proof for the occurrence of Haines jumps in our experiments, we carried out a simple calculation of the theoretical fluid front rate, based on the imposed flow rate and the dimensions of the Clashach sample (see SI Text S1), and compared this with the measured distance of H2 moved between a selection of frames (SI Fig. S7, Table 2). The calculation reveals that where H₂ enters several pores in bursts, the distance travelled per frame is more than two orders of magnitude higher than the theoretical fluid front advance per frame of 0.86 µm (Table 2) and at least more than one order of magnitude higher than the mean pore diameter of 27.5 µm. Acknowledging the simplicity of our calculations and the limitation of dealing with 2D data only, this indicates that Haines jumps are shaping the displacement of brine by H2 during drainage.

Haines jumps contribute to the relative permeability, are the cause for hysteresis in gas retention and make up a significant part of the energy dissipation of the system [22]. Haines jumps have been described frequently in multiphase fluid flow (e.g. [22,64]) but have never previously been demonstrated for H_2 . Recognizing Haines jumps is critical for our understanding of the H_2 and brine two-phase fluid flow in porous rock due to the impact on H_2 recovery from storage reservoirs.

4.4. Correlation to oscillations in pressure

The pressure data collected during the experiments can be used to gain further insight into $\rm H_2$ saturation fluctuations in the pore space, and the evolution of the $\rm H_2$ connectivity with time. Firstly, for the $\rm H_2$ fractional flow of 0.5, the pressure continues to increase long after the $\rm H_2$ saturation, at least in the imaged part of the core, has plateaued (Fig. 2). For earlier times, the pressure is lower, but the $\rm H_2$ saturation is comparable to later times during the experiment. This implies that the mobility of the $\rm H_2$ is higher at earlier times. This observed transition to steady state is comparable to observations made for $\rm N_2/brine$ multiphase injections [62].

For the $\rm H_2$ fractional flow of 0.5, we see pressure oscillations repeating approximately every 2 min (Fig. 2). These are also noticeable in the time-averaged spectral power and can be represented by red noise (red dashed line in Fig. 9c). This is in alignment with previous findings for multiphase flow of $\rm N_2$ and brine [39]. Red noise indicates a stochastic process where pressure fluctuations are seen throughout the pore

Table 2 Measured front progression between selected 2D radiograph frames of H_2 injection into a brine-saturated rock sample at an injection rate of 5 μ l min⁻¹, corresponding to $Nc = 4.25 \times 10^{-9}$ and a continuous fluid front rate per frame of 0.034 mm s⁻¹. The first H_2 appears on frame 39.

Frame interval	Front advance upwards (mm)	Front advance sidewards (mm)	Front advance rate upwards (mm s ⁻¹)	Front advance rate sidewards (mm s ⁻¹)
38-39	0.2	_	8.4	
39-40	0.7	0.4	28	14.8
40-41	0.1	0.2	4	7.2
355-356	0.4	-	16	-
356–357	0.7	0.1	28	4

space, resulting in intermittent filling of pores over a wide range of timescales, from seconds to minutes [39]. We observed H₂ rearrangements on the order of seconds (Fig. 4, Fig. 7) to minutes (Fig. 4), highlighting a cascade of timescales over which dynamics are occurring.

The evolution of the longer frequencies in Fig. 9 differs to pore-scale observations made with N_2 /brine multiphase injection but is comparable to larger, core-scale observations made with N_2 /brine multiphase injection [62]. In Spurin et al. [53] it was concluded that the non-linear dynamics occurred at lower capillary numbers for the larger samples, and this difference was likely due to higher volumes of gas fluctuating due to the changing role of viscous forces. Due to the lower viscosity of H_2 (9.01 µPa s ([40], 298 K and 4.7 MPa) versus 18.9 µPa s for N_2 ([65], 5 MPa and 295 K)), it seems that the dynamics are manifesting differently to the N_2 /water pore-scale experiments even under the umbrella of red noise. Furthermore, the amplitudes in the time-averaged spectral power are higher for the H_2 experiments. The amount of gas moving is larger for the H_2 experiments, with 10 % of the volume fluctuating during steady state, whereas it was 2–3 % for N_2 experiments conducted at a higher N_6 [56,61], thus the amount of dynamics is greater for H_2 .

For the H_2 fractional flow of 0.75, there is a drop-in pressure after 30 min of injection (Fig. 2; counting from time of arrival of the 4:1 H_2 /brine fluid composition in the rock sample), which correlates to the onset of rapid pressure fluctuations. This is reflected in the spectral power of the pressure data in Fig. 9, where shorter periods increase in magnitude at this time. Assuming that event size is linked to event frequency (which was observed for N_2 /brine experiments [39]), an increase in shorter period events should correlate to the formation of smaller ganglia. This can be observed in Fig. 6b and d, where the number of smaller ganglia increases for the scans at 33.7 min and 67 min. However, for the scans at 100.3 min and 133.7 min, there is the creation of 1 larger ganglion. Whether this ganglion breaks up and reconnects would require higher temporal imaging. Further work is required to see if event size is correlated to frequency for H_2 experiments.

It should be noted that the field of view covers around 1/6th of the sample volume (SI Fig. S8). This means that discrete events cannot be fully correlated to fluctuations in the pressure data, as dynamics are occurring outside the field of view.

It is important to consider the internal pressure oscillations of the pumps used in the experiment. In this work the back pressure was via a high-pressure Cetoni pump which adjusts the volume inside its syringe to keep a constant pressure of 5 MPa. Since the pump adjusted the pressure within seconds, and the observed pressure oscillations in steady state injection experiments were on the scale of 2–3 min (Figs. 2 and 9), the oscillations are likely to originate from the pore scale displacement processes.

4.5. Relative and absolute permeability estimations

Steady state injections into Clashach rock during the time-resolved experiments showed~15% lower H2 saturations (Figs. 4 and 5, SI Figs. S2 and S3) and a decrease of the kr by four orders of magnitude at a brine flow fraction of 0.9 compared to values in Thaysen et al. [13]. This notable difference was despite the fact that the rock samples were collected from the same outcrop bulk sample and a similar average porosity was measured (12.5-13.5 % and 13.6 % respectively). While the error ranges on relative permeability measurements using small rock samples applied in µCT studies are high [61,66] and may well span across the observed differences, the distribution of H₂ in the pore space differed between the two studies: In Thaysen et al. [13] it was even and all over the rock (SI Fig. S4), whereas in the current study H2 never entered one section of the rock (SI Fig. S2 and S3; upper right side of the rock). This suggests some heterogeneity in the pore structure of the Clashach sample applied in this study. Added heterogeneity was not evident from the porosity variation along the length of the sample (SI Fig. S9). While generally areas of high porosity correspond to areas of high permeability and low capillary entry pressure [67], porosity

heterogeneity is not always correlated with capillary or permeability heterogeneity [66], which may have been present in our sample. As such permeability variations of two orders of magnitude at only 2 % variations in porosity have been reported in Clashach [68]. Jangda et al. [25] showed that H_2 may bypass areas of Clashach rock with lower permeability, to migrate rapidly along a single channel, lowering the S_{nwi} . When the channel is broken by imbibition, the S_{nwr} may be higher than the S_{nwi} [25]. Considering the small size of rock samples in μ CT-studies, any heterogeneity in the samples is likely to be impactful, and care must be taken when extracting bulk properties from μ CT studies [66]. However, even in rocks with homogeneous porosity and permeability channelizing of the gas plume may be observed as a result of gravitational [67], and viscous forces [26] acting on the system.

From the fractional flow versus saturation curves for H_2 it is evident that H_2 saturation is low at low H_2 /brine injection ratios, and only becomes significant at higher ratios, peaking at a maximum of 50 % saturation for a H_2 fractional flow of 1 for the Clashach sample studied in Thaysen et al. [13] (Fig. 10a). This is as expected from Eq. (6), given the M of H_2 to water, and indicative of a water wet system. The H_2 fractional flow versus saturation curves for Clashach sandstone are in line with previously reported H_2 fractional flow experiments in untreated Vosges sandstone at 5.5 MPa and 20 °C (Fig. 10a) [34]. Compared to CO_2 , H_2 displaces more brine, indicating it is more wetting (Fig. 10a). Previous contact angle comparisons in cleaned pure quartz and hydrophilic silica reported lower wettability of H_2 [69,70], indicating that sample pretreatment, or a lack of the latter as in our studies and in Yekta et al. [34], significantly affects displacement mechanisms.

Hydrogen fractional flow graphs are not directly comparable to H₂ relative permeability graphs (Figs. 10 and 1, respectively) because the former do not consider the S_{wi} of the rock. In reality, the relative permeability of the gas will never be the same as the absolute permeability. Meanwhile, the S_{wi} for Clashach sandstone was determined to 12.6-14.0 % at 0.43 MPa [18], indicating a high kr_{H2} and H₂ storage capacity. A high kr_{H2} would be consistent with results of the unsteady state relative permeability experiments by Rezeai et al. [17] but stands in contrast to relative permeability studies with the steady state technique reporting low kr_{H2} (Fig. 1). In line with this, previously reported LET parameters for a Berea sandstone with low kr_{H2} differ to the ones reported for Clashach in this study (Table 2). Very similar fractional flow graphs as in Yekta et al. [34] (Fig. 10) and further comparison with the low kr_{H2} results from the same study (Fig. 1), both obtained on a rock sample of only slightly bigger size than in our experiments (61 mm length and 15 mm diameter), suggests that the real kr_{H2} in Clashach sandstone is lower than what is estimated based on the fractional flow graph.

The estimated absolute permeability of 35 mD was an order of magnitude lower than experimentally determined permeabilities of 122–178 mD in larger Clashach cores [18,68]. Absolute permeability estimations on a small sample are subject to increased uncertainty related to the weaker differential pressure across a small rock core and a higher impact of any heterogeneities in smaller samples relatively to larger ones [66].

4.6. Processes or experimental conditions that may have affected the

4.6.1. Dissolution

Dissolution of H_2 into non- H_2 -equilibrated brine may manifest as an elevated water saturation at the core inlet at low H_2 fractional flows [32], an increase in disconnected H_2 ganglia further down the core as the H_2 partial pressure drops and H_2 is coming out of the solution [32] and/or an increase in S_{nwr} relative to when H_2 -equilibrated brine is injected [16]. Those effects were not observed within the field of view of the sample, however it neither covered the inlet nor the close-to-outlet region of the rock (SI Fig. S8). Meanwhile Thaysen et al. [13], using the same injection conditions and field of view as in this study, found

that the H_2 saturation and H_2 pore occupancy deviated only 0.02 % from the initial value after a 10-hour lock-in period after injection stop, indicating negligible dissolution.

4.6.2. Effect of the viscosity difference between brine and hydrogen in steady state injections

In steady state injections with H_2 and brine, the two fluids will enter pores preferentially based on the difference in capillary pressure of the fluids. For any given pressure condition and flow rate, the brine should enter pores more readily due to its more than two orders of magnitude higher viscosity $(1.247 \times 10^{-3} \, \text{Pa} \, \text{s} \, \text{at 5 MPa}$ for the brine [71] and $9.01 \times 10^{-6} \, \text{Pa} \, \text{s} \, \text{at 298 K and 4.7 MPa}$ for H_2 [65]) that increases the Nc (more viscous forces). This effect will be reflected in the observed H_2 saturations and connectivity. In a real reservoir, the injection-induced brine flow rates will vary locally, reflecting a range of capillary numbers that will not always be in favour of preferential entry of brine.

4.6.3. Pressure and temperature

This study used a pore fluid pressure of 5 MPa and ambient temperature, which is lower than for many real-world aquifers. At the time of writing the effect of pressure and temperature on $\rm H_2$ fluid flow dynamics is not elucidated. Existing studies on the effect of pressure on the wettability, the primary control on multiphase fluid flow [72], show discrepancy [18]. A comparison of μ CT studies on $\rm H_2$ fluid flow in sandstone (Table 1) indicates little effect of pressure on the S_{nwi} . Further investigation is needed to determine whether the applied experimental conditions constitute a limitation to the prediction of the $\rm H_2$ fluid flow at higher pressure and temperature.

5. Conclusions

Real-time imaging of steady state injections of H_2 and brine into Clashach sandstone provided insights into the evolution of the H_2 saturation and connectivity in the pore space at different H_2 fractional flows. A higher H_2 fractional flow of 0.75 relative to 0.5 increased the H_2 saturation in the pore space from 20–22 % to 28 %, suggesting a lower H_2 storage capacity in sandstone aquifers with higher injection-induced hydrodynamic flow. Contrary to our hypothesis and to previous findings for oil at high capillary numbers of 10^{-4} to 10^{-6} [55], H_2 connectivity was weak and remained similar across different H_2 fractional flows. This indicates little influence of connectivity on pore space H_2 saturation during steady state flow and suggests a low H_2 recovery from sandstone aquifers with injection-induced hydrodynamic flow, which may adversely affect the economic feasibility of the H_2 storage operation. Future studies should attempt to μ CT-image H_2 and brine injections at a higher resolution to confirm observations of low H_2 connectivity.

Intermittent flow pathways were observed in minor parts of the rock during macroscopically steady state flow. Intermittent flow has not previously been observed at low capillary numbers of 4.7×10^{-9} and was most likely caused by the high viscosity ratio of the H2-brine system relative to previous studies reporting intermittency in N2-brine and oilbrine fluid flow, e.g. [55,56,60,61]. Dynamic fluid rearrangements are outside the framework of Darcy's law extended to multiphase flow. However, the evolution of H2 saturation with H2 fractional flow could still be described using the conventional framework of relative permeability functions, suggesting that the large-scale movement of H2 was not affected by intermittent flow. Estimations of the H2 relative permeability based on Darcys law and using the fractional flow data indicated relatively high permeability relative to previous studies in similar systems but predictions of gas injectivity and recovery should be made with caution due to the neglection of the irreducible water saturation in these estimations and the small size of the rock sample in our experiments.

The fraction of intermittent H_2 flow to constant pathway flow is likely to increase at flow rates corresponding to higher capillary numbers, as shown previously for N_2 [62]. Considering the lower

viscosity ratio of the $\rm H_2\textsc{-}brine$ system compared to the $\rm N_2\textsc{-}brine$ system, relatively more intermittent flow can be expected for $\rm H_2$ for a given flow rate and shifts in the $\rm H_2$ relative permeability in response to increasing intermittent flow can be expected at lower capillary number than for $\rm N_2$ (i.e. $<0.38\textsc{-}1.1\times10^{-6}$ [62]). Future experiments should measure the volume of $\rm H_2$ fluctuating intermittently as a function of capillary number and fractional flow to allow the quantification of the increase of intermittent flow with increasing capillary number as well as a determination of the capillary number at which intermittent flow will affect macroscale flow behaviour such as the relative permeability. To model intermittent flow alongside laminar flow, new reservoir models incorporating Navier-Stokes equations may have to be developed.

Unsteady state injections of H_2 into a brine saturated rock were captured with live 2D radiography to provide insights on dynamic fluid processes that occur over timescales of $10 \text{ s}{-}100 \text{ s}$ of milliseconds. The radiographs showed that H_2 enters the brine-saturated rock within seconds, dispersing in bursts, also known as Haines jumps. Haines jumps have been studied extensively using oil, CO_2 or air as nonwetting phase, e.g. [22,73–75], but have not previously been reported for H_2 . Haines jumps are important energy-dissipating pore-scale events that are the cause of hysteresis and hence affect non-wetting phase retention in rock. Yet common reservoir models lack consistent links to these elementary pore-scale displacement processes. Future research should assess techniques to scale these events for improved reservoir modelling of H_2 injectivity and storage efficiency. This will be pivotal not only for underground H_2 storage applications but extends to areas such as natural H_2 exploration and subsurface H_2 farming.

Author contributions

The experimental kit was built by Butler and Thaysen. Experiments were carried out by Thaysen, Butler, Hassanpouryouzband, Freitas. Alvarez-Borges and Atwood were the supporting beamline scientists during the experiments at Diamond Light Source. Image reconstruction and analysis was carried out by Thaysen and Rizzo. Data were visualized by Thaysen. Interpretation of the results was by Thaysen, Butler, Hassanpouryouzband and Spurin. The original draft of the manuscript was written by Thaysen, with contributions and review from Butler, Hassanpouryouzband, Freitas, Edlmann, Alvarez-Borges, Rizzo and Spurin. All authors have given approval to the final version of the manuscript.

CRediT authorship contribution statement

Eike M. Thaysen: Writing – original draft, Visualization, Methodology, Investigation, Formal analysis, Conceptualization. Ian B. Butler: Writing – review & editing, Supervision, Methodology, Investigation, Conceptualization. Aliakbar Hassanpouryouzband: Writing – review & editing, Methodology, Investigation. Catherine Spurin: Writing – review & editing, Visualization, Formal analysis. Damien Freitas: Writing – review & editing, Investigation. Roberto Rizzo: Writing – review & editing, Methodology. Fernando Alvarez-Borges: Writing – review & editing, Investigation, Data curation. Robert Atwood: Investigation. Katriona Edlmann: Writing – review & editing, Funding acquisition.

Declaration of competing interest

The authors declare that they have no known competing financial interests or personal relationships that could have appeared to influence the work reported in this paper.

Acknowledgment

Thaysen, Butler, Hassanpouryouzband and Edlmann gratefully acknowledge the funding support from the Engineering and Physical Science Research Council (EPSRC) HyStorPor project [grant number EP/

S027815/1] and from the Fuel Cells and Hydrogen Joint Undertaking (JU) under grant agreement no. 101006632. The JU receives support from the European Union's Horizon 2020 research and innovation programme and Hydrogen Europe and Hydrogen Europe Research. Freitas is supported by an AFOSR/EOARD grant (FA8655-21-1-7005). This work was enabled and carried out with the support of Diamond Light Source, Beamline I12-JEEP 101006632 (proposal mg26730-1). We would like to thank Thomas Connolley for any correspondence and help with setting up the experiments at Diamond Light Source, and Samuel C. Krevor at Imperial College for helpful discussions around the data visualization and interpretation.

Appendix A. Supplementary data

Supplementary data to this article can be found online at https://doi.org/10.1016/j.jcis.2025.137704.

Data availability

Data can be downloaded from University of Edinburgh Datashare under https://doi.org/10.7488/ds/7913.

References

- E.M. Thaysen, et al., Effect of dissolved H2SO4 on the interaction between CO2rich brine solutions and limestone, sandstone and marl, Chem. Geol. 450 (2017) 31–43.
- [2] E.M. Thaysen, et al., Effects of lime and concrete waste on vadose zone carbon cycling, Vadose Zone J. 13 (11) (2014) 1–11.
- [3] S.O. Snæbjörnsdóttir, et al., Carbon dioxide storage through mineral carbonation, Nat. Rev. Earth Environ. 1 (2020) 90–102.
- [4] IPCC, IPCC report Global Warming of 1.5 C: Summary for Policymakers, 2018.
- [5] L. Stalker, et al., Communicating leakage risk in the hydrogen economy: Lessons already learned from geoenergy industries, Front. Energy Res. 10 (2022) 1–15.
- [6] S. Krevor, H. de Coninck, S.E. Gasda, N.S. Ghaleigh, V. de Gooyert, H. Hajibeygi, R. Juanes, J. Neufeld, J.J. Roberts, F. Swennenhuis, Subsurface carbon dioxide and hydrogen storage for a sustainable energy future, Nat. Rev. Earth Environ. 4 (2023) 102–118.
- [7] C.R. Matos, J.F. Carneiro, P.P. Silva, Overview of large-scale underground energy storage technologies for integration of renewable energies and criteria for reservoir identification, J. Energy Storage 21 (2019) 241–258.
- [8] N. Heinemann, et al., Enabling large-scale hydrogen storage in porous media: the scientific challenges, Energ. Environ. Sci. 14 (2021) 853–864.
- [9] E.M. Thaysen, et al., Microbial risk assessment for underground hydrogen storage in porous rocks, Fuel 352 (128852) (2023) 1–12.
- [10] A. Hassanpouryouzband, et al., Geological hydrogen storage: geochemical reactivity of hydrogen with sandstone reservoirs, ACS Energy Lett. 7 (2022) 2203–2210.
- [11] A. Aftab, A. Hassanpouryouzband, A. Martin, J.E. Kendrick, E.M. Thaysen, N. Heinemann, J. Utley, M. Wilkinson, R.S. Haszeldine, K. Edlmann, Geochemical Integrity of Wellbore Cements during Geological Hydrogen Storage, Environ. Sci. Technol. Lett. 10 (7) (2023) 551–556.
- [12] E.M. Thaysen, et al., Estimating microbial growth and hydrogen consumption in hydrogen storage in porous media, Renew. Sust. Energ. Rev. 151 (111481) (2021) 1–15.
- [13] E.M. Thaysen, et al., Pore-scale imaging of hydrogen displacement and trapping in porous media, Int. J. Hydrog Energy 48 (8) (2023) 3091–3106.
- [14] M.J. Veshareh, E.M. Thaysen, H.M. Nick, Feasibility of hydrogen storage in depleted hydrocarbon chalk reservoirs: Assessment of biochemical and chemical effects, Appl. Energy 323 (119575) (2022) 1–11.
- [15] N. Heinemann, et al., Hydrogen storage in saline aquifers: The role of cushion gas for injection and production, Int. J. Hydrog Energy 46 (2021) 39284–39296.
- [16] Z. Jangda, et al., Pore-scale visualization of hydrogen storage in a sandstone at subsurface pressure and temperature conditions: trapping, dissolution and wettability, J. Colloid Interf. Sci. 629(Part B) (2022) 316–325.
- [17] A. Rezaei, et al., Relative permeability of hydrogen and aqueous brines in sandstones and carbonates at reservoir conditions, Geophys. Res. Lett. 49 (12) (2022) 1–9.
- [18] E.M. Thaysen, I.B. Butler, Z. Jangda, H. Menke, K. Singh, K. Edlmann, Hydrogen wettability and capillary pressure in Clashach sandstone for underground hydrogen storage, J. Energy Storage 97 (2024).
- [19] N. Heinemann, M. Wilinson, K. Adie, K. Edlmann, E.M. Thaysen, A. Hassanpouryouzvband, R.S. Haszeldine, Cushion gas in hydrogen storage—a costly CAPEX or a valuable resource for energy crises? Hydrogen 3 (4) (2022) 550-563
- [20] M. Lysyy, G. Ersland, M. Fernø, Pore-scale dynamics for underground porous media hydrogen storage, Adv. Water Resour. 163 (104167) (2022) 1–13.
- [21] R.T. Armstrong, et al., Multiscale characterization of wettability in porous media, Transp. Porous Media (2021).

- [22] S. Berg, H. Ott, S.A. Klapp, A. Schwing, R. Neiteler, N. Brussee, A. Makurat, et al., Real-time 3D imaging of Haines jumps in porous media flow, PNAS 110 (10) (2013) 3755–3759.
- [23] N.K. Jha, et al., Pore scale investigation of hydrogen injection in sandstone via X-ray micro-tomography, Int. J. Hydrog. Energy 46 (2021) 34822–34829.
- [24] A. Al-Yaseri, et al., Snap-off effects and high hydrogen residual trapping: implications for underground hydrogen storage in sandstone aquifer, Energ Fuel 38 (4) (2024) 2983–2991.
- [25] Z. Jangda, et al., Subsurface hydrogen storage controlled by small-scale rock heterogeneities, Int J Hydrog Energy 60 (2024) 1192–1202.
- [26] Y. Zhang, B. Bijeljic, Y. Gao, S. Goodarzi, S. Foroughi, M.J. Blunt, Pore-scale observations of hydrogen trapping and migration in porous rock: demonstrating the effect of ostwald ripening, Geophys. Res. Lett. 50 (e2022GL102383) (2023).
- [27] S. Goodarzi, et al., Trapping, hysteresis and Ostwald ripening in hydrogen storage: A pore-scale imaging study, Int. J. Hydrog Energy 56 (2024) 1139–1151.
- [28] S. Higgs, et al., Direct measurement of hydrogen relative permeability hysteresis for underground hydrogen storage, Int. J. Hydrog Energy 50 (2024) 524–541.
- [29] S. Goodarzi, et al., Ostwald ripening leads to less hysteresis during hydrogen injection and withdrawal: A pore-scale imaging study, Int. J. Hydrogen Energy 114 (2025) 475–485.
- [30] M. Boon, H. Hajibeygi, Experimental characterization of H2/water multiphase flow in heterogeneous sandstone rock at the core scale relevant for underground hydrogen storage (UHS), Nat. Sci. Rep. 12 (14604) (2022) 1–11.
- [31] M. Lysyy, et al., Hydrogen relative permeability hysteresis in underground storage, Geophys. Res. Lett. 49 (2022) 1–8.
- [32] M. Boon, et al., Multiscale experimental study of H2/brine multiphase flow in porous rock characterizing relative permeability hysteresis, hydrogen dissolution, and Ostwald ripening, Sci. Rep. 14 (1) (2024) 30170.
- [33] A., Ebrahimiyekta Characterization of geochemical interactions and migration of hydrogen in sandstone sedimentary formations: application to geological storage, Université d'Orléans, 2017.
- [34] A.E. Yekta, et al., Determination of hydrogen-water relative permeability and capillary pressure in sandstone: application to underground hydrogen injection in sedimentary formations, Transp. Porous Med. 122 (2) (2018) 333–356.
- [35] F. Lomeland, Overview of the LET family of versatile correlations for flow flunctions, in International Symposium of the Society of Core Analysts, Trondheim, Norway, 2018.
- [36] B.T. Ngwenya, S.C. Elphick, G.B. Shimmield, Reservoir sensitivity to waterflooding: an experimental study of seawater injection in North Sea reservoir analogs, AAPG Bull. 79 (1995) 285–304.
- [37] Y.T.F. Chow, G.C. Maitland, J.P.M. Trusler, Interfacial tensions of (H2O + H2) and (H2O + CO2 + H2) systems at temperatures of (298–448) K and pressures up to 45 MPa, Fluid Ph. Equilib. 475 (2018) 37–44.
- [38] Y.T.F. Chow, G.C. Maitland, J.P.M. Trusler, Erratum to "Interfacial tensions of (H2O + H-2) and (H2O + CO2 + H-2) systems at temperatures of (298–448) K and pressures up to 45 MPa", Fluid Ph Equilib 503 (112315) (2020) 1.
- [39] C. Spurin, et al., Red noise in steady-state multiphase flow in porous media, Water Resour. Res. 58 (7) (2022) e2022WR031947.
- [40] E. Yusibani, et al., A capillary tube viscometer designed for measurements of hydrogen gas viscosity at high pressure and high temperature, Int. J. Thermophys. 32 (6) (2011) 1111–1124.
- [41] S. Iglauer, et al., Comparison of residual oil cluster size distribution, morphology and saturation in oil-wet and water-wet sandstone, J Colloid Interf Sci 375 (2012) 187–192.
- [42] M. Drakopoulos, et al., I12: the Joint Engineering, Environment and Processing (JEEP) beamline at Diamond Light Source, J. Synchrotron Radiat. 22 (3) (2015) 828–838.
- [43] T. Pak, Saturation tracking and identification of residual oil saturation, University of Edinburgh, 2014.
- [44] T. Pak, et al., Droplet fragmentation: 3D imaging of a previously unidentified porescale process during multiphase flow in porous media, PNAS 112 (7) (2015) 1947–1952.
- [45] S. Higgs, et al., In-situ hydrogen wettability characterisation for underground hydrogen storage, Int. J. Hydrog Energy 47 (26) (2022) 13062–13075.
- [46] 46. Vlassenbroeck, J., et al., Octopus 8: A high performance tomographic reconstruction package for X-ray tube and synchrotron micro-CT, in Advances in Xray tomography for geomaterials, J. Desrues, G. Viggiani, and P. Bésuelle, Editors, ISTE: London, UK, 2010.
- [47] R.E. Rizzo, et al., Using internal standards in time-resolved X-ray micro-computed tomography to quantify grain-scale developments in solid-state mineral reactions, Solid Earth 15 (4) (2024) 493–512.
- [48] A.L. Herring, et al., Effect of fluid topology on residual nonwetting phase trapping: Implications for geologic CO2 sequestration, Adv. Water Resour. 62 (2013) 47–58.
- [49] J. Schindelin, et al., Fiji: an open-source platform for biological-image analysis, Nat. Methods 9 (7) (2012) 676–682.
- [50] S.C. Krevor, et al., Relative permeability and trapping of CO2 and water in sandstone rocks at reservoir conditions, Water Resour.. Res. 48 (W02532) (2012) 1–16.
- [51] A.A. Taha, A. Hanbury, Metrics for evaluating 3D medical image segmentation: analysis, selection, and tool, BMC Med. Imag. 15 (1) (2015) 29.
- [52] R.A. Ketcham, W.D. Carlson, Acquisition, optimization and interpretation of X-ray computed tomographic imagery: applications to the geosciences, Comput. Geosci. 27 (4) (2001) 381–400.
- [53] C. Spurin, et al., Pore-scale fluid dynamics resolved in pressure fluctuations at the darcy scale, Geophys. Res. Lett. 50 (18) (2023) e2023GL104473.

- [54] H.J. Vogel, U. Weller, S. Schlüter, Quantification of soil structure based on Minkowski functions, Comput. Geosci. 36 (10) (2010) 1236–1245.
- [55] R.T. Armstrong, et al., Beyond Darcy's law: The role of phase topology and ganglion dynamics for two-fluid flow, Phys. Rev. E 94 (4) (2016).
- [56] C.A. Reynolds, H. Menke, M. Andrew, S. Krevor, Dynamic fluid connectivity during steady-state multiphase flow in a sandstone, PNAS 114 (31) (2017) 8187–8192.
- [57] M. Rücker, et al., The effect of mixed wettability on pore-scale flow regimes based on a flooding experiment in ketton limestone, Geophys. Res. Lett. 46 (6) (2019) 3225–3234.
- [58] M. Rücker, et al., From connected pathway flow to ganglion dynamics, Geophys. Res. Lett. 42 (10) (2015) 3888–3894.
- [59] S. Zou, et al., Experimental and theoretical evidence for increased ganglion dynamics during fractional flow in mixed-wet porous media, Water Resour. Res. 54 (5) (2018) 3277–3289.
- [60] Y. Gao, et al., X-ray microtomography of intermittency in multiphase flow at steady state using a differential imaging method, Water Resour. Res. 53 (12) (2017) 10274–10292
- [61] C. Spurin, et al., The development of intermittent multiphase fluid flow pathways through a porous rock, Adv. Water Resour. 150 (2021).
- [62] C. Spurin, T. Bultreys, B. Bijeljic, M.J. Blunt, S. Krevor, Mechanisms controlling fluid breakup and reconnection during two-phase flow in porous media, Phys. Rev. E 100 (4) (2019) 043115.
- [63] M.J. Blunt, Multiphase flow in permeable media. A Pore-scale perspective, Cambridge University Press, Cambridge, United Kingdom, 2017.
- [64] K. Singh, et al., Dynamics of snap-off and porefilling events during two-phase fluid flow in permeable media, Sci. Rep. 7 (5192) (2017) 1–13.
- [65] E. Yusibani, et al., A capillary tube viscometer designed for measurements of hydrogen gas viscosity at high pressure and high temperature, Int. J. Thermophys. 32 (6) (2011) 1111–1124.

- [66] M.H. Krause, S.M. Benson, Accurate determination of characteristic relative permeability curves, Adv. Water Resour. 83 (2015) 376–388.
- [67] M. Seyyedi, M.B. Clennell, S.J. Jackson, Time-lapse imaging of flow instability and rock heterogeneity impacts on CO2 plume migration in meter long sandstone cores, Adv. Water Resour. 164 (2022).
- [68] I.O. Ojala, B.T. Ngwenya, I.G. Main, Loading rate dependence of permeability evolution in porous aeolian sandstones, J. Geophys. Res. Solid Earth 109 (B1) (2004).
- [69] S. Iglauer, A. Muhammad, A. Keshavarz, Hydrogen wettability of sandstone reservoirs: implications for hydrogen geo-storage, Geophys. Res. Lett. 48 (3) (2020) 1–5.
- [70] C. Chen, J. Xia, H. Bahai, Effect of the temperature on interfacial properties of CO2/H2 mixtures contacting with brine and hydrophilic silica by molecular dynamics simulations, Energy Fuel 37 (23) (2023) 18986–18995.
- [71] T. Nakai, et al., Effect of pressure on the viscosity B coefficient of cesium chloride in water, Mater. Sci. Res. Int. 2 (3) (1996) 143–147.
- [72] N.R. Morrow, Wettability and its effect on oil recovery, J. Pet. Technol. 42 (12) (1990) 1476–1484.
- [73] T. Bultreys, et al., Real-time visualization of Haines jumps in sandstone with laboratory-based microcomputed tomography, Water Resour. Res. 51 (10) (2015) 8668-8676
- [74] K.R. Tekseth, D.W. Breiby, 4D imaging of two-phase flow in porous media using laboratory-based micro-computed tomography, Water Resour. Res. 60 (4) (2024) e2023WR036514.
- [75] I. Zacharoudiou, E.S. Boek, J. Crawshaw, The impact of drainage displacement patterns and Haines jumps on CO2 storage efficiency, Sci. Rep. 8 (1) (2018) 15561.